MEASUREMENT OF SURFACE HEAT FLUX DUE TO FIN-INDUCED SHOCK-BOUNDARY LAYER INTERACTIONS

A Thesis

by

JOHN M. WIRTH

Submitted to the Graduate and Professional School of
Texas A&M University
in partial fulfillment of the requirements for the degree of

MASTER OF SCIENCE

Chair of Committee,	Rodney Bowersox
Committee Members,	Edward White
	Waruna Kulatilaka
Head of Department,	Ivett Leyva

December 2021

Major Subject: Aerospace Engineering

ABSTRACT

In high-speed flows, fins cause shock-boundary layer and shock-shock interactions that result in complicated, 3D flow fields, with heating being the primary concern to vehicle designers and engineers. A methodology has been developed to study fin-induced shock-boundary layer interactions (SBLI) at Texas AM University. Wind tunnel models were 3D printed from Formlabs Rigid 10K resin using a Formlabs 3L printer. To accurately quantify heating caused by fins, a new method was developed to convert infrared temperature measurements into heat flux using the full, 3D heat equation. The fin-cone model with a single, highly swept fin on a 7° half-angle cone was printed and tested, replicating the same pressure frequency spectra and heat flux patterns as measured on PEEK and stainless steel models in other wind tunnels and computational simulations. Multi-fin models comprised of interchangeable conical and ogive fore-bodies paired with 3 or 4 fin cylindrical rear-sections were used to generate shock-boundary layer interactions in the Actively Controlled Expansion Tunnel and Mach 6 Quiet Tunnel at Texas A&M University. Experiments on blockage models of the multi-fin geometries were used to lay the groundwork for CFD and stability analysis validation studies. Infrared data mapping to the solution domain was demonstrated to be accurate within the mesh resolution and the solutions were found to be converged for mesh density. Model alignment studies found that the number of and location of vortex structures could be affected by less than 1° of misalignment. Increasing unit Reynolds number supported stronger SBLI, with more secondary vortices and higher heating levels. These effects seemed to dominate any differences due to model geometry. The 3D heat flux tool was found to be limited in that peak heating often occurred at sharp corners, requiring larger meshes than could be supported to fully resolve those geometric features. Additionally, the data processing time for the entire process averaged at least one day per run if started entirely from scratch and processed in series. Overall, the 3D, heat flux reduction tool reduced the discrepancy between old 1D tools and CFD by 50% on the fins and prepare the way for simultaneous infrared and pressure studies of SBLI on multi-fin geometries.

ACKNOWLEDGMENTS

I would like to thank Dr. Bowersox for taking me on as a student and guiding me through this research, as well as Dr. White and Dr. Kulatilaka for their help on my committee. Additionally, I am indebted to my teammates, Dr. Travis Kocian for his excellent work generating CFD and stability results and Jacob Vaughn and Lisa Brown for helping with wind tunnel model construction. Finally, this thesis would not have been possible without the support of my fellow graduate students at the NAL and their relentless efforts to help me make these experiments work.

CONTRIBUTORS AND FUNDING SOURCES

Contributors

This work was supported by a thesis committee consisting of Professors Rodney Bowersox (advisor) and Edward White of the Department of Aerospace Engineering and Professor Waruna Kulatilaka of the Department of Mechanical Engineering. Portions of this research were conducted with the advanced computing resources provided by Texas A&M High Performance Research Computing.

Computational fluid dynamics work for the multi-fin models was completed by Dr. Travis Kocian. The models were in part designed and printed by Dr. White's group, including Lisa Brown and Jacob Vaughn. All other work was completed independently by the author.

Funding Sources

Research was sponsored by the Army Research Office and was accomplished under Cooperative Agreement Number W911NF-19-2-0243. The views and conclusions contained in this document are those of the authors and should not be interpreted as representing the official policies, either expressed or implied, of the Army Research Office or the U.S. Government. The U.S. Government is authorized to reproduce and distribute reprints for Government purposes notwithstanding any copyright notation herein.

NOMENCLATURE

ACE	Actively Controlled Expansion Tunnel
AoA	Angle of Attack
CFD	Computational Fluid Dynamics
DAQ	Data Acquisition
DNS	Direct Numerical Simulation
IR	Infrared
M6QT	Mach 6 Quiet Tunnel
MATLAB	Matrix Laboratory Software
NAL	National Aerothermochemistry and Hypersonics Laboratory
PSD	Power Spectral Density
SBLI	Shock-Boundary Layer Interaction
SLA	Steriolithography (3D Printing Method)
TAMU	Texas A&M University
α	Thermal diffusivity
γ	Ratio of specific heats
ρ	Density
c	Specific heat
k	Thermal conductivity
M	Mach number
Pr	Prandtl number
q	Heat flux
T_{aw}	Adiabatic wall Temperature

T_w	Wall Temperature
ΔT	Temperature above initial temperature
∞	Freestream values

TABLE OF CONTENTS

Page

LIST OF FIGURES

FIGURE Page

LIST OF TABLES

TABLE Page

1. INTRODUCTION

1.1 Motivation

The minimum requirement of any aircraft designer is to design a vehicle that can be controlled, generate enough lift, and overcome whatever drag is incurred. The implicit assumption is that the vehicle also survives the flight, which is usually the case in lower-speed flight if a vehicle meets those three requirements. However, at sufficiently high speeds, vehicle heating becomes a primary concern of the designer. Control surfaces can become points of concern for the designer, who must ensure that they do not cause heating that would threaten the vehicle.

1.2 Background

The flow field around a vehicle flying at high speeds can quickly become complicated, but any analysis must start by simplifying it into its components. First, along any object traveling in any flow, there is a thin boundary layer where viscosity slows the flow to zero velocity relative to the aircraft at the surface. Second, any turning or compression of a supersonic flow as it goes along a solid body will result in a shock wave. Now, in a purely supersonic flow, shocks are relatively easy to analyze because disturbances can only propagate downstream. On a real vehicle, however, both the boundary layer and shocks exist. The complicated interactions whereby the effects of the shock travel back upstream through the boundary layer and affect the structure of the shock itself are generally referred to as Shock-Boundary Layer Interactions (SBLI). They pose a quandary for aerodynamicists due to their nonlinear, self-interacting nature as well as the implications they can have on the survivability of a vehicle.

Experimental work in the middle of the last century outlined the general structure of fin-induced SBLI, starting from the most basic SBLI. The 2D SBLI is generated by a compression ramp, like those on engine inlets. In the flow outside the boundary layer, an inviscid analysis shows that a shock forms as the flow turns to get around the obstruction, with a static pressure increase across the shock, which is transmitted through the boundary layer. This creates an abrupt, adverse pressure

gradient, resulting in reversed flow next to the surface and a separation bubble contained in the boundary layer [3]. The supersonic flow outside of the boundary layer must turn to get around this aerodynamic obstruction, resulting in a shock coming off of the front of the separation bubble. The flow expands as it goes around the separation bubble until it must straighten out when it again encounters the vehicle surface, resulting in a reattachment shock, which converges with the separation shock to form the inviscid shock. This results in the classic lambda shock structure [4]. The reattachment shock causes increased heating because the separated flow is energized by the freestream and compressed by two shocks before interacting with the surface. Work by Chapman et al. showed that this is a free interaction when the incoming boundary layer is turbulent, meaning the extent of the interaction is governed by the Mach number, state of the incoming boundary layer, and the wall temperature only [5].

More complicated SBLI were also surveyed in the middle of the 20th century to give an idea of the flows which may be caused by any protuberance from a vehicle. These 3D SBLI act in many ways like their 2D counterparts, with mass suction modeling the effects of an additional dimension [6]. These 3D SBLI can be generally characterized into a couple of basic flows. A cylinder on a flat plate was found to generate a lambda shock structure at the front, with the "mass suction" converting the recirculation bubble into a horseshoe vortex as it is swept around the cylinder. This SBLI also seems to be a free interaction, with the extent of upstream influence decreasing as the cylinder was thinned and swept back [4]. Corner flow was found to generate a conical flowfield, with the compression caused by the presence of a boundary layer on each face generating two shocks that eventually converged [7, 8]. The effects of the cylinder on a flat plate and a corner flow can be combined to generate a fin-induced flowfield, as sketched in Figure 1.1. Vortices are generated from the recirculation region, which causes higher heating and pressure streaks corresponding to the reattachment lines and secondary vortices being generated inside the separation region for strong enough interactions [6]. These studies laid much of the groundwork for studies of fin-induced SBLI, but computational approaches became necessary to further probe these flow fields.

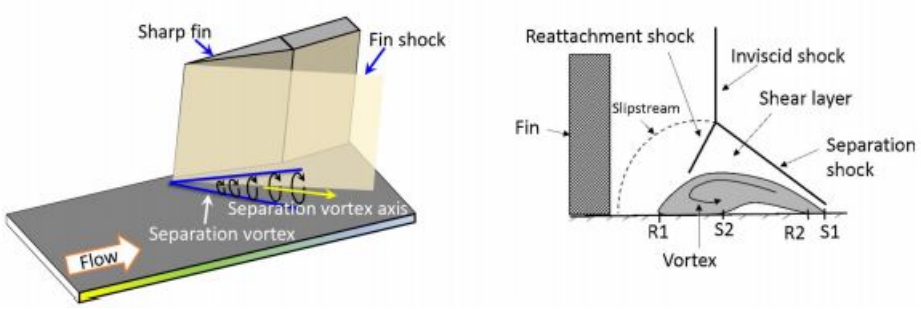

Figure 1.1: Basic structure of a fin-induced SBLI (Reprinted from [1]).

Simulating SBLI computationally has historically been quite challenging. First, the problem is fundamentally unsteady and turbulence modeling may not capture the necessary physics to simulate an SBLI [9]. At the turn of the century, large eddy simulations (LES) were thought to be the way forward, but have not since proved to be the solution [9]. Additionally, computational models must be validated by experiments, which have historically not been targeted towards validation and have neglected to collect the details required for the computations. Due to the complexity of SBLI, these studies warrant close collaboration between experimentalists and computationalists [10].

Turbulence greatly adds to the complexity of simulating SBLI. The first solution to this problem is to simulate laminar flows. Studies of laminar SBLI confirmed that the flow is conical some distance downstream of the SBLI, like the turbulent SBLI, with only slight modifications to the extent of the upstream influence [11, 6, 5]. This study found that the separated streamline did not reattach, but that an energetic vortex dragged other streamlines to the surface [11]. This probing of the flow field would have been difficult for early experimentalists to accomplish. For turbulent boundary layers, simulations have been carefully validated by experiments. K-omega turbulence models were able to capture the correct number of separations and reattachments in a Mach 2.5 flow over a 20° fin [12]. These methods were then used to show that the horseshoe vortex caused by a fin on an axisymmetric body experiences 3D pressure relief, resulting in a curved path rather than a straight line as on a flat plate [12].

Most recently, close collaboration between computationalists and experimentalists has been useful in the development of stability analysis codes that attempt to predict transition to turbulence.

The EPIC code developed at TAMU is one such code that first solves a laminar basic state of a flow before using the linear and nonlinear parabolized stability equations to track the growth of disturbances introduced into the boundary layer [13]. Measurements on a cone at an angle of attack in Mach 6 flow were used to validate the base flow field and the growth of disturbances inside crossflow vortices predicted by the EPIC code [14, 13]. A similar analysis was conducted for the 2nd mode on a flared cone [15, 16]. These combined efforts promise to quickly develop codes that can predict transition for a certain number of known instabilities, a long-time goal of aerodynamicists.

Recent efforts have turned these tools towards fin-induced SBLI. Unlike the 2nd mode and crossflow instabilities, fin-induced SBLI generate complex flow fields with many types of instabilities. The fin-cone geometry was the basis of one of the most detailed of these studies. Initial surveys were conducted to understand the effects of fin sweep, fin thickness, and nose-tip radius, both experimentally and computationally [17, 18]. After these parameters were understood, simultaneous heat flux and surface pressure measurements were conducted on the final configuration, which was a 16 inch long, 7° half-angle cone with a 1/4 inch thick fin swept to 75° [19]. Unlike previous SBLI studies, the fin-cone was found to produce a leading edge vortex system that caused multiple heating streaks on the fin, in addition to the horseshoe vortex system on the conical body which was expected from previous studies on cylindrical bodies [19]. These vortices are created by crossflow due to the pressure gradient supported by the compression of the freestream onto the conical surface [20]. They are susceptible to secondary instabilities, due to their inflectional velocity profile [20]. The measurement of these secondary instabilities has been measured on other geometries [21]. Additionally, the vortex alters the thickness of the boundary layer, leading to a variation of the 2nd mode frequency [22]. Computational base states were probed with dynamic mode decomposition for possible instabilities at different locations in the flow and were validated by predicting a 180 kHz vortex instability on the surface at a unit Reynolds number of $7 \times 10^6 m^{-1}$, which was measured in the experiments [23, 19]. This provides the most comprehensive study of a fin-induced SBLI, with the basic flow field including a horseshoe vortex that curves along the

axisymmetric surface due to 3D pressure relief, a leading edge vortex on the fin itself, and computational and experimental data of the heating and pressure fluctuations caused by the horseshoe vortex system. Measurement of heat flux on the fin itself proved elusive.

There are significant challenges associated with conducting experiments for SBLI that can be used to validate computational models. These experiments require wind tunnel models that can be used to simultaneously measure heat flux and surface pressure fluctuations. This has typically been done by precisely machining stainless steel and PEEK models, which can get quite expensive, especially when multiple configurations need to be tested [19, 24]. This leaves experimentalists in want of a less expensive model manufacturing technique. The disturbances to be measured can be quite sensitive to model alignment, and therefore model manufacturing quality, with just the 2nd mode changing frequency up to 80 kHz per degree on a flared cone [25]. The SBLI themselves can also be quite sensitive to alignment, with the heating front of a 2D separation bubble shown to drastically vary across a flared cone within 1° of perfect alignment [26]. The models therefore must have some type of alignment apparatus that can be fine-tuned in situ to achieve perfect alignment with the freestream, and experiments will likely involve a significant amount of time aligning the models. Even with the model adequately manufactured and aligned, the effects of the freestream can be significant. Studies of a cylinder on a flat plate in a conventional tunnel showed significant dependence of the SBLI on freestream pressure fluctuations [27]. Any vortex generated by the SBLI is susceptible to receiving freestream disturbances due to the inflectional velocity profile [20]. Quiet facilities have been developed to study transition by other mechanisms [28]. However, these facilities can only accommodate models designed for use in those facilities, unlike the cylinder on a plate [27]. These are issues that must be resolved or understood to allow for comparison with computations.

Once sufficient experimental accuracy has been achieved, data must be gathered, with heating due to SBLI being the primary quantity of interest in most cases. The measurement of heating can be quite tricky. Heat-flux gauges have been used to measure heat flux directly at a couple of locations with only 6% error compared to other methods [24]. However, in other cases heat-flux gauges

have been found to have almost 20% error compared to theoretical values [29]. Thermocouples could be used to measure temperature and then convert it into heat flux, but like heat flux gauges, limit the results to a sparse number of sensors, with the vast majority of the model undetermined. Thermally sensitive paint has been used successfully to get global temperature measurements, although it adds uncertainty because application of the paint can add thickness to the model [17]. Infrared (IR) thermography has been quite successful at accurately resolving temperature profiles of models, particularly at TAMU [30, 31, 24]. However, these global temperature measurements must be converted to heat flux by post-processing in order to be useful.

Because of the extreme conditions of hypersonic flight, ground facilities cannot adequately replicate all physics of flight. One of the most critical of these shortcomings is true temperature conditions, with longer-duration wind tunnels often operating at much colder than flight conditions. As a result, temperature data in cold tunnels must be converted to nondimensional heat flux for adequate comparison to flight. This can be done by solving the heat equation in the wind tunnel model and extracting the gradients at the surface to find heat flux based on Fourier's law. This has historically been done through a number of simplifying assumptions. For thermocouple measurements, a finite-domain, 1D heat equation solver named QCALC was developed to solve for heat flux on a flat plate, with adaptations made for cylindrical and spherical bodies [32]. Studies of the method found that errors tend to grow with time when the geometry of the model does not exactly fit the assumed geometry [32]. An IR data reduction scheme based on QCALC was developed for IR thermography at TAMU, with a finite-difference scheme being used to solve the 1D heat equation at each pixel, rather than at each thermocouple [27]. This code was found adequate even for curved geometries [33]. A study of crossflow vortex heating on the HIFiRE-5 geometry using IR thermography has been conducted using the 1D equation in cylindric coordinates, but a 3D analysis was recommended since strong gradients existed in directions besides the wall-normal [34]. It is important to note that as flows get more complicated, the underlying assumptions in these methods become less and less valid and more complicated data reduction techniques become necessary.

Besides the simplifying assumptions made to the heat equation, the numerical technique used for estimating heat flux can be important. A study found that, especially in short-duration, blow-down tunnels, unsteadiness in the flow due to tunnel startup and strong gradients can cause numerical instabilities in heat flux [35]. These are due to the estimation of heat flux by computing gradients over numerical data, which will amplify any noise or errors. The suggested solution was to use a quasi-inverse solution method, guessing the heat flux, solving the heat equation for the surface temperatures, and using an optimization technique to find the heat flux that gives the measured surface data [35]. This technique has been put into practice at Purdue and seems to generate good results [36]. The necessity of this technique is unclear, due to the widespread use of finite-difference techniques with adequate results.

1.3 Objectives

The objectives of this research are to:

1. Demonstrate reliable, rapid, affordable construction of wind tunnel models for simultaneous infrared and installed sensor measurements.

2. Demonstrate reduction of infrared temperature measurements into heat flux over 3D geometries using the full, 3D heat equation.

3. Provide experimental results for various geometries to provide a basis for future experimentation of SBLI's, closely collaborating with computational partners to work towards providing a database for the validation of CFD and stability analysis tools.

2. EXPERIMENTAL METHODS

2.1 Facilities

The experiments were conducted in the sister tunnels at the NAL, the Actively Controlled Expansion (ACE) Tunnel and the Mach 6 Quiet Tunnel (M6QT). The tunnels were set up in parallel between a tank of filtered, dry air pressurized to 2500 psi and a double ejector system capable of pulling a vacuum to 3 Torr. Run times were limited to 30 seconds by the mass flow through the ejector system, though in many cases this was more than sufficient. Prior to a typical run, the tunnels and upstream infrastructure were preheated to 430 K using an industrial heater. During the run, this was the stagnation temperature in the settling chamber, corresponding to a static temperature of approximately 55 K in the test section, just above the liquefying temperature of oxygen.

The key difference between the two tunnels lay in the levels of freestream disturbances. ACE was a conventional facility designed to provide excellent optical access to the test section. This made it an excellent facility for recording infrared images over large portions of the models. For unit Reynolds numbers above $3 \times 10^6 m^{-1}$ it had noise levels (defined as fluctuations over mean pressure, $\frac{p'}{\bar{p}}$) of approximately 1.5%, lower than most other conventional facilities. ACE had a variable area diffuser, which allowed some tuning of the Reynolds number range based on each model. The multi-fin models were reliably run at unit Reynolds numbers of $2.5 - 7.5 \times 10^6 m^{-1}$ while the fin-cone achieved $2.5 - 7 \times 10^6 m^{-1}$.

The M6QT was designed to have a quiet core of flow at approximately Mach 6 and unit Reynolds numbers of $6 - 11.5 \times 10^6 m^{-1}$. This core was a double-conic section, sketched in Figure 2.1, bounded at the upstream end by the last characteristic of the expanding flow, after which Mach 6 flow is achieved. It achieved this core by first removing upstream disturbances through a long settling chamber, straightening the flow with a series of increasingly finer meshes, and then allowing the mesh-induced vorticity to dissipate before bleeding off the settling chamber boundary

layer to start a new boundary layer at the nozzle contraction. Then, the flow expanded through a highly polished nozzle, to delay transition by surface roughness, with a long, straight expansion section to reduce the strength of Gortler vortices. Regardless of the efforts, the boundary layer on the nozzle wall transitioned to turbulence, sending pressure fluctuations along Mach lines into the freestream flow, bounding the quiet core on the downstream end.

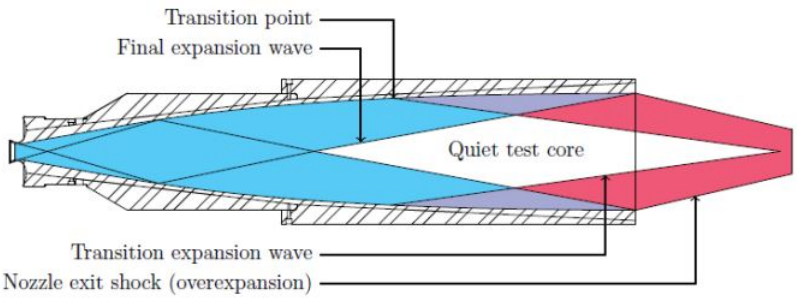

Figure 2.1: Quiet core in the M6QT (Reprinted from [2]).

Several challenges were added to experiments in the M6QT due to the measures taken to achieve a quiet core of flow. The nozzle of the quiet tunnel, which contained the entirety of the quiet core, had no optical access. In order to reduce the risk of damage to the nozzle as well as increase the amount of space available to mount models and sensors, the nozzle was housed in a free-jet test section. Due to the operating conditions, the nozzle flow was overexpanded when compared to the ambient pressure of the test section, leading to the formation of a compression shock at the exit of the nozzle. This created a downstream bound to the Mach 6 flow that also had to be respected. Finally, the freestream impinged on the bell-mouth diffuser before entering the ejector. The M6QT worked by generating enough quiet flow ($\frac{p'}{\bar{p}} < 0.1\%$) in the core of the nozzle that instabilities formed in the tunnel model boundary layer at the front of the model have space to grow and dominate instabilities due to freestream noise, all while having enough of the model outside of the nozzle to measure IR data at locations of interest, but not enough to interact with the compression shock, and creating a flowfield that will not unstart at the fixed area diffuser.

These constraints had easily been met by conical-type models in the past. However, the models used to study SBLI's are much more complex and certain features and interactions of interest did not occur in the quiet core due to these additional constraints. To better inform the results, a new characterization of the M6QT freestream was conducted.

2.1.1 M6QT Freestream Flow Characterization

The freestream flow of the M6QT was originally characterized by Dr. Jarrod Hofferth upon the establishment of the facility. Using a pitot-traverse system, he mapped out the noise and Mach number for a sweep of unit Reynolds number on the centerline and two, constant unit Reynolds numbers throughout the center plane of the nozzle, parallel to the floor of the test section [25]. Researchers after Dr. Hofferth have replicated his results at specific locations for their models to verify that they match the initial survey [31, 30]. The following characterization extended the initial survey to include a 3D survey of the nozzle flow as well as extending the range of frequencies included in power spectral densities of the freestream disturbances.

The 3D traverse used to complete the characterization was built by Dr. Alex Craig and a complete description of the system can be found in his dissertation [2]. The traverse allowed movement in cylindrical coordinates and was compatible with several sensors and pitot probes, as long as they could fit into the adapter. The adapter was connected by two rails and a threaded rod to the carriage which contained three motors to move in the three directions. The carriage was mounted to a circular rail that allowed 205° motion. To facilitate the entire range necessary for the survey, short and long rails were used to extend the adapter to the correct radial distance. The long rails were observed to be more flexible when fully extended and more prone to fluttering during preheat and tunnel shutdown.

Two pitot probes were used to collect pressure data. The short pitot, shown in the traverse in Figure 2.2, was built and used in a previous study and was 14 cm long with a Kulite XCEL-100-10A. It was used to collect data at the exit plane of and exterior to the nozzle. The long pitot was constructed by the author to extend into the nozzle. A Kulite XCEL-100-15A was secured inside a series of stainless steel tubes to ensure the straightness and rigidity of the 40 cm-long probe.

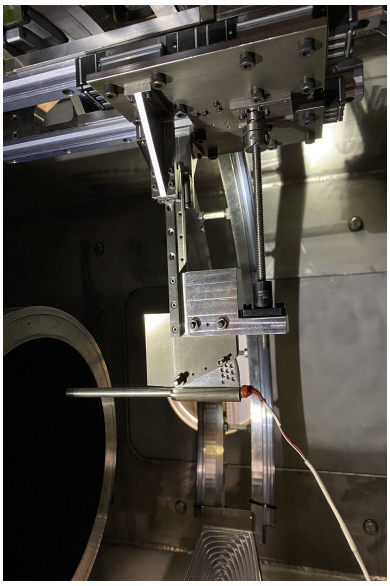

Figure 2.2: The short pitot at the exit plane

The freestream survey measured pressure fluctuations throughout the upper back portion of the nozzle and across a range of unit Reynolds numbers. Based on the limitations of the traverse and tunnel run time, the pitot was held at a constant radius and axial distance and was swept 180° in 20° increments across the top of the nozzle. The unit Reynolds number was held at a constant $10 \times 10^6 m^{-1}$ to match the most extreme run conditions required for the experiments. Lower Reynolds numbers were assumed to have lower noise levels and a larger extent of the quiet core. For the centerline, the Reynolds number was swept from 7.5-12 $\times 10^6 m^{-1}$, with the $10 \times 10^6 m^{-1}$ point being used to complete the spatial map. Table 2.1 shows the list of locations that were measured at any axial location.

Axial Location (cm)	Radii (cm)
70	0, 2, 4, 6
80	0, 2, 4, 6
90	0, 2, 4, 6
101 (Exit)	0, 2, 4, 6, 8
111	0, 2, 4

Table 2.1: Pitot locations for M6QT freestream survey.

For signal processing, the Kulite signal was passed through an in-house processing box before being passed to a National Instruments USB-6366 Data Acquisition box where it was sampled at 1 MHz for 200 ms per point. The lack of filtering allowed for the measurement of the resonant frequency of the Kulites, which were 246 kHz and 258 kHz for the short and long pitot probes respectively. This information proved valuable for the use of a new KSC-2 Kulite box in a concurrent verification study. The 200,000 samples at each point were converted into power spectral densities (PSD) using Welch's method via a Hamming window with 50% overlap and 2^{11} points per window. To obtain noise levels, the PSDs were integrated using a simple Riemann sum to 200 kHz, simulating a low-pass filter at 200 kHz. Integration to 50, 100, and 150 kHz showed convergence using this method while remaining out of the influence of the resonant frequencies.

Mach number contours were extracted from the Kulite data by taking the average voltage and converting them to pressures via a linear calibration, performed after the tunnel tests. The calibration of the long pitot was performed in the HXT by vacuuming down the test section to known pressures and measuring the voltage output. The same technique was attempted for the short pitot, but it had ceased to work in the time intervening between the tunnel tests and the calibration. The centerline run at the exit plane was used to calibrate the short pitot, assuming the centerline Mach number was 5.87, the centerline Mach value at x/L = 0.8 and 0.9. The Mach number contours at the exit plane and outside the nozzle are therefore less certain than those inside the nozzle.

2.2 Wind Tunnel Models

Wind tunnel models had the requirements of being suitable for infrared (IR) thermography as well as surface pressure measurements. They were manufactured using a Formlabs 3L, SLA printer with Rigid 10K resin. This greatly reduced the price and production time of each model when compared to machined steel and polyether ether ketone (PEEK) models that are typically used for infrared thermography. The first models were blockage models of the multi-fin geometries printed at Formlabs and tested pre-release of the 3L printer and Rigid 10K resin. The use of new manufacturing materials and methods required original quantification of some material properties as well as design iterations to ensure model quality.

2.2.1 Thermal Properties Characterization

Thermal properties of the Rigid 10K resin necessary for IR data reduction were determined by hot disk analysis using a Thermtest transient plane source system and a 5464 nickel alloy sensor. The nickel alloy sensor was a double spiral inside of a Kapton cover. During the experiment, the sensor was sandwiched between two samples and electric current was passed through it. The resistance of the double spiral directly correlated to its temperature and the voltage was used to determine power. From the temperature, power, and time to take 200 samples, thermal conductivity was determined. Given the density of the material, specific heat was determined as well. These three quantities define the thermal diffusivity of the material, which was necessary to solve the heat equation and determine heat flux.

For this study, five different material samples were cut from the fin of an extra blockage model for the analysis, due to the printer and resin still being pre-release. The hot disk analysis measured thermal diffusivity normal to the fin surface, perpendicular to the print direction, which was deemed to be the most important because the models were the thinnest in that direction. The material was assumed to be isotropic in the heat flux analysis. The samples were sized to be 4 mm thick and at least 20 mm wide to cover the entire sensor with room to spare. The thickness constrained the test time because heat from the nickel sensor could not have time to be transmitted completely through the sample, allowing for a mathematical assumption that the sensor was in an infinite medium. Power and run time were varied throughout the test with time in between the runs to allow the sample temperature to equilibrate, but the run time eventually settled to 10 seconds with 50 mW of power. Different samples were traded in and out to ensure the largest possible sample of printed material. After the hot disk analysis, the samples were all measured and weighed to give density. The material properties of the Rigid 10K resin post-cure are shown in Table 2.2 below.

Thermal Conductivity (W/m*K)	Density (kg/m^3)	Specific Heat (J/kg*K)
0.5337	1655	939.8

Table 2.2: Thermal properties of Rigid 10K printed models

The low thermal conductivity made the Rigid 10K suitable for infrared thermography. Heat transferred to the model from the flow was radiated and observed before it diffused through the model, allowing heating patterns on the surface to closely correspond to the flow field. It should be noted that it had more than twice the thermal conductivity of PEEK but at a much more affordable price.

2.2.2 Multi-Fin Geometries

Multi-fin geometries, defined in Figure 2.3, were constructed to have interchangeable, 10-inch fore- and fin-bodies, leading to rapid testing of several configurations. Both fore-bodies had a spherical nose tip with a radius of 0.125 in. One fore-body was an ogive and one was conical between the nose-tip and joint with the fin section, testing the difference between boundary layers formed in favorable pressure gradients versus those without a pressure gradient. One fin-body had 3 fins while the other had 4 to gauge the effects of distance on fin-fin interactions. The fins were thin and swept at 80°. Fin thickness and sweep were not considered as parameters for this study.

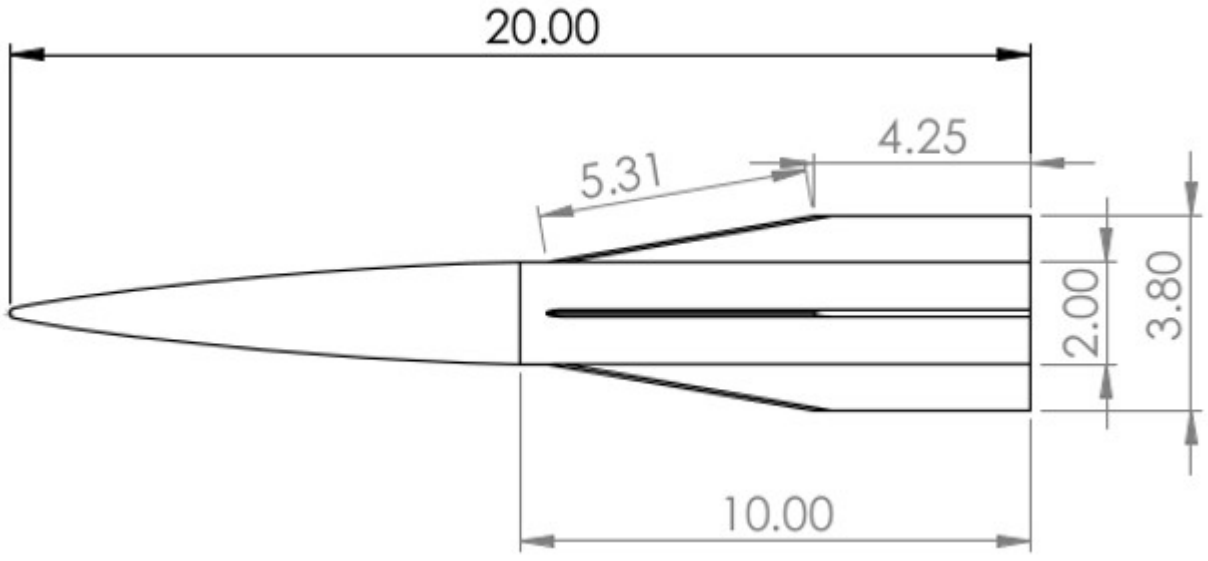

Figure 2.3: Dimensions (in inches) of multi-fin models, ogive and 4-fin bodies depicted.

Most of the data for this thesis were collected using the blockage models of the multi-fin ge-

ometries, depicted in Figure 2.4. They were printed pre-release of the 3L printer by Formlabs and hand-finished before use in the tunnel. These models had known imperfections which created uncertainty in the results. The models proved useful for developing and testing data reduction methods as well as informing improvements in future model design and manufacturing.

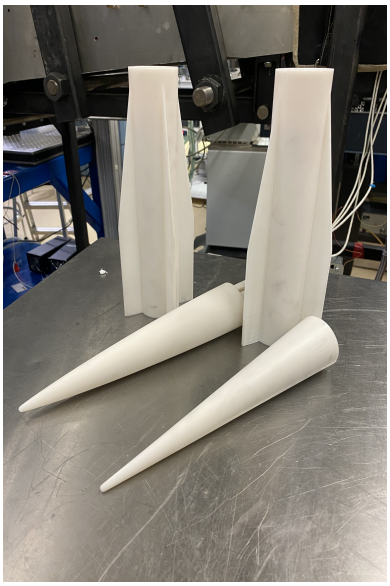

Figure 2.4: Blockage models, from top to bottom, left to right: the 4-fin and 3-fin bodies, ogive and straight fore-bodies.

Improved designs and models have been created to fix some of the issues with the preliminary models. First, the fore-body-to-fin-section joint has been improved to create a symmetric joint with repeatable alignment, meaning the orientation between the two parts is exactly the same from run to run. A gap of approximately 50 microns with less than a 10-micron step between the interchangeable parts was achieved. Second, an alignment piece, shown in Figure 2.5, was printed to interface between the mounting spar and the model. Threads were directly printed into the adapter piece and the models that allowed four screws to connect the adapter to the model and the model to the spar. The 3D printing process was found incapable of getting a perfect surface on the side of the print that was attached by supports to the base plate. The adapter piece was designed to

join those faces together, allowing shims to correct any imperfections. Additionally, the alignment of the model can be varied by the use of shims and the tightening of the four alignment screws. Any misalignment or natural loosening of the model due to heating and cooling during and between experiments could be quickly readjusted. Finally, the overall quality of the print was improved, requiring no hand-finishing and reducing the concern of model-induced asymmetries.

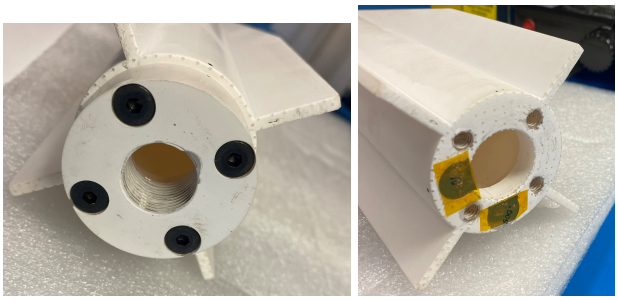

Figure 2.5: Adapter piece on improved models for alignment.

2.2.3 Fin-Cone

To validate the methodology, the fin-cone was manufactured, tested, and the data processed in the same manner as the multi-fin geometries. Results could be compared to experimental results from Purdue, DNS results from Minnesota, or basic state results from TAMU [19, 23, 18]. The model was a 7° half cone with a 1/4-inch thick fin, swept at 75°, commencing 4 inches from the beginning of the model. To print the fin section as a single piece, the model was made 15 inches long, with a 4-inch nose section and an 11-inch fin section, and instrumented with PCB 132B38's 31° from the fin on both sides 33 cm along the axis from the nose of the model. The SLA printing process was able to achieve a 150-micron diameter nose-tip and a 50-micron gap between the nose-tip and the body of the model. Figure 2.6 depicts the model.

Pressure sensors were used to find the frequencies of instabilities at the surface and ensure that the manufacturing of the fin-cone was adequate to replicate results from other studies. The PCBs on the fin-cone were powered by manufacturer in-line signal conditioners and low-pass filtered at 1

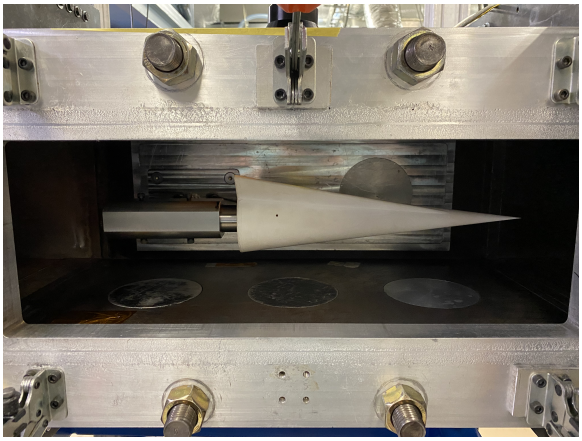

Figure 2.6: Fin-cone model installed in ACE.

MHz before being passed to a National Instruments USB-6366 DAQ where they were sampled at 2 MHz. PSDs were calculated using Welch's method via a Hamming window with 50% overlap and 2^{10} points per window. These PSDs were sufficient to identify instabilities and determine model alignment.

2.3 Infrared Thermography

Infrared (IR) thermography was conducted using a FLIR SC8000 camera. The camera had several integration times from which to choose, which is the amount of time that the aperture is open, with longer integration times having less error and a lower maximum temperature. A 50 mm zoom lens was used in the M6QT while a 17 mm lens was used in ACE, due to the free-jet test section moving the camera much further from the model. Fish-eye lens distortion was accounted for when using the 17 mm lens but was negligible for the zoom lens. Wind tunnel models were installed after the tunnels were preheated to 430 K and recording started just before the tunnels were started, allowing for the measuring of initial temperatures and isolating heating due to aerodynamic effects from heating due to being in a preheated tunnel.

A MATLAB application was created to analyze the data, combining several features that had previously been used at the National Aerothermochemistry and Hypersonics Laboratory (NAL) as well as adding some new utilities. Existing software resources at the NAL read the raw IR data

into MATLAB where it could be post-processed. Automatically, the first five frames were averaged together and subtracted from every frame, giving the change in temperature ΔT, which was the temperature used for heat flux analysis to reduce errors based on initial conditions, reflections, lens anomalies, etc., although the actual temperature data was stored for use in nondimensionalization. The IR data was automatically synchronized with the tunnel data acquisition (DAQ) system by matching up the tunnel unstart time, which results in a spike in temperature across the entire model and a drop in Mach number as measured by the DAQ. The user then had several post-processing options. The image could be de-warped depending on the lens used, the image cropped and/or scaled, and averages could be taken over time or space to compress and smooth the data. The data could then be displayed as a video of ΔT at each pixel or processed into heat flux using the analysis shown in sections 2.3.1 and 2.3.2.

2.3.1 Heat Flux Analysis

Temperature data collected in ground facilities must be converted into heat flux before comparison to other facilities or flight tests. Heat flux in a continuum is proportional to the temperature gradient, defined in equation 2.1 below, where k is the thermal conductivity of the wind tunnel model. In this case, the gradient normal to the surface at the surface is assumed to be due entirely to aeroheating. Heat flux can be nondimensionalized into the Stanton number using the specific tunnel conditions measured during each tunnel run.

$$q = -k * \frac{\partial T}{\partial n} \tag{2.1}$$

$$St = \frac{q}{\rho c_p U (T_{aw} - T_w)} \tag{2.2}$$

The adiabatic wall temperature is calculated assuming the laminar boundary layer recovery factor. The recovery factor is found to be close to constant even in turbulent regions and boundary layers in ACE and M6QT tend to be laminar unless purposely tripped.

$$T_{aw} = T_{\infty}(1 + \sqrt{Pr}\frac{\gamma - 1}{2}M_{\infty}^2) \tag{2.3}$$

Converting infrared temperature measurements into heat flux requires finding a transient solution to the conductive heat equation in the wind tunnel model, where infrared measurements provide temperature boundary conditions on the surface of the domain. Once the transient solution is found for the entire run, gradients at the surface can be converted into heat flux. The full, 3D heat equation is listed as equation 2.4 where α is the thermal diffusivity of the solid. For experiments with 3D flows and geometries, the transient solution to that equation can be found using the methods outlined in section 2.3.2. The author will refer to results from this method as 3D heat flux. In many experiments, heat flux in directions other than the wall-normal direction is negligible and it is more efficient to use a 1D, simplified equation. Both solution methods take advantage of the linearity of the heat equation. The entire domain is initialized to zero, and the change in surface temperature during the tunnel run is used to solve the heat equation, isolating heat flux due to aeroheating from other heating that may occur.

$$\frac{\partial T}{\partial t} = \alpha * \nabla^2 T \tag{2.4}$$

The solution to the 1D heat flux equation was found using a forward-time, central-space finite-difference numerical method. The value of each pixel represents one boundary condition of a 1D string that extended 1/4 inch into the model normal to the image plane, with the other boundary condition assumed to be 0, since the heat from the air did not have time to penetrate that distance during the run. The solution to each pixel was found simultaneously and independently. The heat flux was then extracted using a 2nd-order, forward difference approximation for the temperature gradient and Fourier's law. Heat flux was displayed at each pixel and the image scaling was used to relate pixels to locations on the geometry.

$$\Delta T_{x,t+1} = (\alpha\frac{\Delta t}{\Delta z^2})(\Delta T_{x-1,t} - 2\Delta T_{x,t} + \Delta T_{x+1,t}) + \Delta T_{x,t} \tag{2.5}$$

where

$$\Delta T = T - T_{init} \tag{2.6}$$

$$q_t = -\frac{k}{\Delta z}(-1.5\Delta T_{0,t} + 2\Delta T_{1,t} - 0.5\Delta T_{2,t}) \tag{2.7}$$

2.3.2 3D Heat Analysis

Many of the assumptions used in the analysis via the 1D heat equation were inapplicable in the case of more complicated geometries. Unlike the flat plates and elliptic cones that had been studied in the past, the models used to generate SBLI's generated complex, 3D flow fields and had fins that were simply too thin for the 1D depth assumption to be accurate. For these geometries, the full 3D heat equation needed to be solved. The MATLAB PDE Toolbox was selected to make a fluid transition between 1D and 3D analyses. The thermal solver used a finite element method to solve the transient heat equation numerically over a domain defined by the visible portion of the model. Mathematically, the 1D, finite difference solution should be quite similar to the 3D, finite element solution, but many more steps were required in data processing to make that happen. Ultimately, the goal was to make improvements above the performance of the 1D analysis and simplifying assumptions were made based on that goal.

Defining the domain over which to solve the 3D heat equation was a balance between solution time and accuracy. Scaling images of the wind tunnel model in situ were used to create CAD models of just the portion that could be seen in the IR. This assumed that no heat flux is conducted to or from parts of the model that can not be seen, but was just as good as the 1D heat flux analysis being conducted at each pixel. Additionally, the thickness of the CAD was truncated to the expected depth of heat penetration throughout the run. Minimizing the domain size paid even more dividends in the 3D analysis than in the 1D. This CAD would then be imported to MATLAB where an unstructured finite element mesh would be generated, with the maximum and minimum spacing between nodes being defined by the user. Ideally, each node in the mesh should correspond to one pixel in the data so as not to lose data. However, meshes of that density may be too large to

run and spatial averaging may be used to get a one-to-one ratio.

Once the mesh was generated, boundary and initial conditions were specified. Just as in the 1D case, the initial condition would be set to zero. The IR data were used as transient boundary conditions on visible surfaces and assumptions were made elsewhere. The faces truncating the extent of the domain into the model were defined as adiabatic, either because of symmetry or because of lack of time for heat to penetrate to that depth in the wind tunnel model. Faces on the invisible sides of fins were set to be symmetric to the visible face. Ultimately, a two-camera system would be more accurate, but in lieu of sufficient information, this was shown to be better than an adiabatic assumption. Finally, all visible surfaces were given transient boundary conditions by mapping the temperatures from the IR data.

The mapping of IR data to the 3D domain proved to be one of the more time-consuming processes, but inevitably so given the complexity of the models. Although the IR data was mapped to a 3D finite element mesh, the problem was really a 2D to 2D mapping from the node to the pixel it corresponded to, due to each node being constrained to be on a surface. The process is outlined in Figure 2.7. Scaling shots were taken with markers at critical locations, determined to be the joints between the fins and the body, around the exterior of the fins, and a couple of points to show the curvature of the body. In a meticulous process, each marker was identified by the user creating a mapping between pixel row and column and x and y coordinates, considering the nose of the model to be the origin. A linear, 2D scattered interpolation was then created to fill in the spaces between the markers. When the solver needed the temperature at a node, it took the coordinates of the node and used the interpolation to find the corresponding pixel.

A variety of outputs could be taken from the solution output. Heat flux could be calculated at each node by taking the dot product of the temperature gradients and normal vectors, already produced during the solution process at each node. Stanton number could be calculated by using the same map on the raw temperature data, stored away by the application. At any point, the mapping could be used in reverse to produce a video like the raw IR video, except with heat flux instead of temperature. This functionality was kept to correspond to the images produced in past

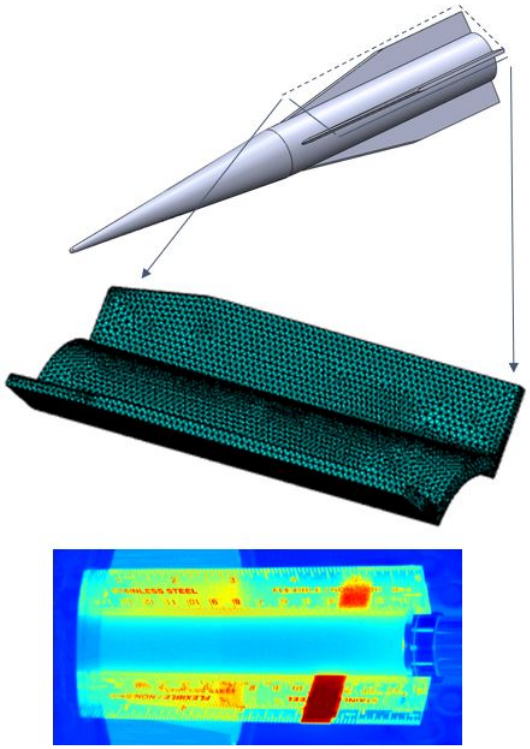

Figure 2.7: Map generation, including CAD modeling, mesh generation, and scaling images with locations clearly identified.

experiments. However, the heat flux at each node was more easily compared to CFD by simply selecting different locations on the model to compare and taking the heat flux results from those nodes.

3. RESULTS

3.1 M6QT Freestream Flow Characterization

The characterization of the M6QT freestream captured Mach numbers, freestream noise levels, and power spectral densities (PSDs) of the freestream noise throughout the freestream. The results confirmed the performance on the center plane as established by Hofferth in 2013 while expanding knowledge of nozzle performance into three dimensions and to higher frequencies of the freestream disturbances [25].

3.1.1 Mach Numbers

Mach number contours, shown in Figure 3.1, were the primary measure of tunnel performance. They revealed a fairly uniform core at approximately Mach 5.9 inside the nozzle. The last characteristic lines were apparent at x/L = 0.7, with the flow at the outer rim not quite getting to its fully accelerated state. The largest extent of the Mach 5.9 core was measured at x/L = 0.8. After this location, the core began collapsing due to the presence of the nozzle wall boundary layer. Notably, the core decelerated more on the center plane than at the top of the nozzle, but the maximum measured variation was only Mach 0.06 (1%) inside the nozzle. Outside of the nozzle, there was much more variation. Excluding the measurement at $\frac{r}{r_{exit}} = 0.2$, which was more of an indicator of tunnel startup than steady Mach number, the maximum variation outside the tunnel was Mach 0.3. The region outside of the nozzle was probably highly unsteady as well, due to the compression shock and shear layer generated as the overexpanded nozzle flow entered the free-jet test section.

3.1.2 Noise Levels

Noise levels measured during the M6QT freestream survey confirmed that the nozzle was still performing as originally characterized, that the freestream noise was axisymmetric, and that the entire nozzle lost quiet flow at a unit Reynolds number of $11.5 \times 10^6/m$ [37]. All data from SBLI were collected below this unit Reynolds number. Plots of noise at several axial locations are shown in Figure 3.2. Due to the slenderness of the pitot and the cylindrical traverse, some mechanical

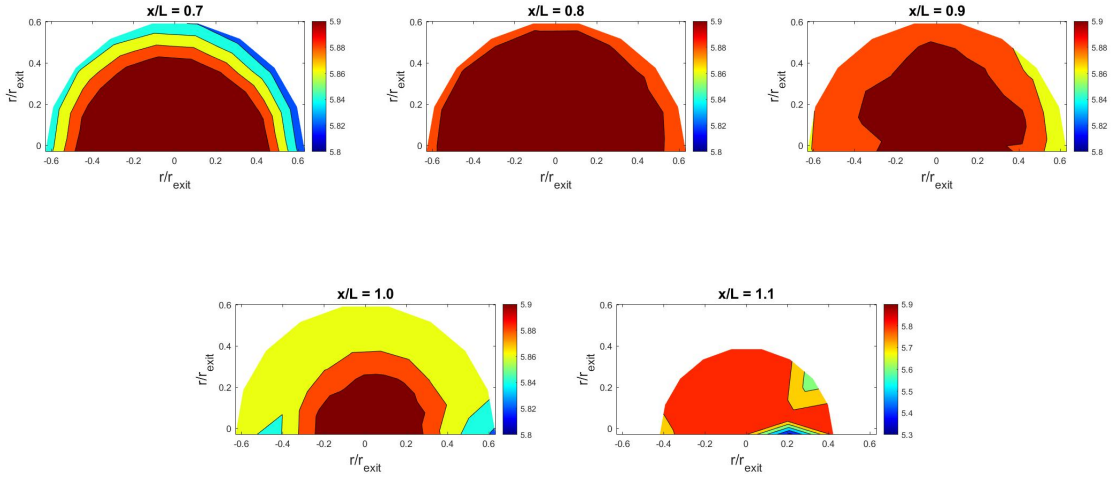

Figure 3.1: Mach number contours in planes normal to nozzle axis at $Re/m = 10{\times}10^6$, perspective is looking upstream into the nozzle.

noise was believed to be introduced during data collection. This flutter was likely worse during startup, leading to slightly higher levels of noise at the beginning of the run, which shows up as higher noise on the far side of the nozzle from the controls, on the right side of the contour maps. The noise was roughly uniform outside of the nozzle. Figure 3.3 shows the loss of quiet flow at $Re/m = 11.5 \times 10^6/m$.

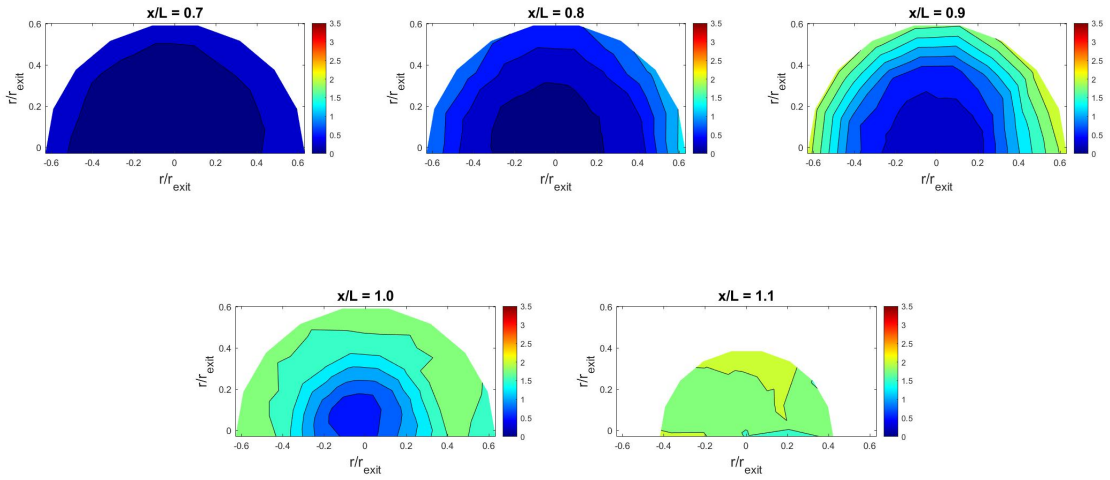

Figure 3.2: Noise contours ($\frac{p'}{\bar{p}}$, %) in planes normal to nozzle axis at $Re/m = 10^{\times}10^{6}$.

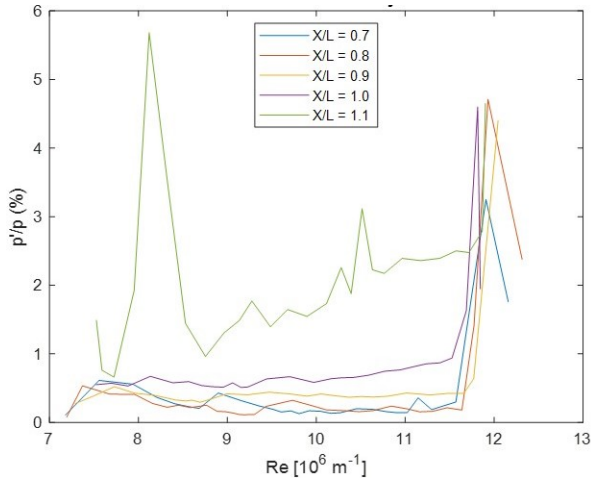

Figure 3.3: Centerline traces of freestream noise level showing total nozzle wall transition at $Re/m = 11.5 \times 10^{6}$.

The placements of the models were chosen to maximize the amount of the model visible to the IR camera while keeping forward of the compression shock from the nozzle exit, as shown in Figure 3.4. This corresponded to the placement of other models of similar length and also ensured that the nose of the model did not extend upstream of the last nozzle characteristic and into lower Mach number flow [37]. On the conical models that the tunnel was designed to study, this had ensured that enough of the model was in the quiet core to let disturbances grow in the boundary layer such that boundary layer transition would be dominated by those disturbances before significant freestream noise would be introduced. On the fin-cone, this held somewhat true, with the fin-induced SBLI being generated in the quiet core. Notably, the fin-cone was run at unit Reynolds numbers less than $10 \times 10^6 m^{-1}$ and the quiet core extended further back on the model than depicted. For the multi-fin models, this was true only of the forebodies. The fin emerged from the cylinder about halfway between the x/L = 0.8 and x/L = 0.9 planes, at a radial distance of $r/r_{exit} = 0.26$, meaning the SBLI and the horseshoe vortex experience 0.75% noise or greater along its entire length. This was an important factor to consider when comparing CFD and experiments on the multi-fin models.

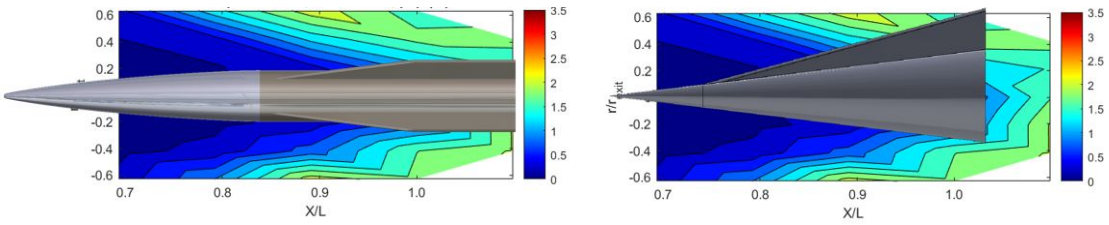

Figure 3.4: Model placement with respect to noise levels on the center plane at $Re/m = 10 \times 10^6$.

3.1.3 Power Spectral Densities

The PSDs of the disturbances in the tunnel were also collected as outlined in the methods section. Contour plots were made by averaging the PSDs of all 10 points at a single radius, shown in Figure 3.5. Those PSDs were plotted using a color map to display intensity, with the frequency

of the disturbance on the x-axis and the axial location of the data on the y-axis. The plots show increased intensity with increasing axial distance, with the majority of the noise coming from less than 50 kHz. The resonant frequencies of the two sensors can easily be seen near 250 kHz. The standard practice of filtering out the resonant frequency was forgone to allow dual-use of the data for other experiments on Kulite data processing. While the magnitudes are incorrect, this did allow the discovery of two peaks at 140 and 225 kHz, which appear when the overall noise approaches 0.75%. These frequencies would be present on the entirety of the SBLI on the multi-fin models.

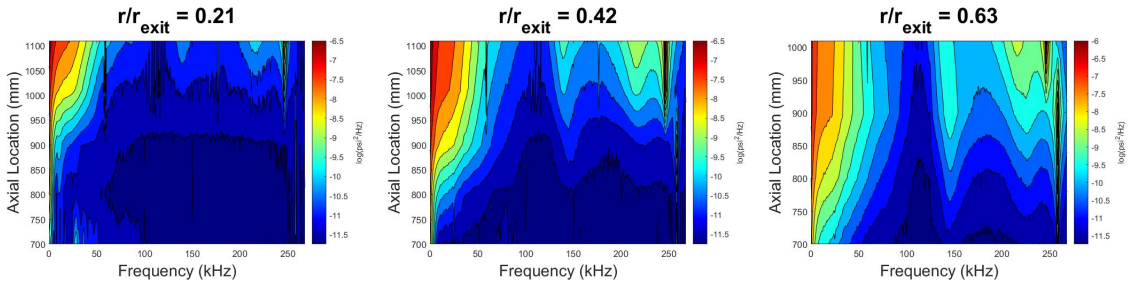

Figure 3.5: Variation of average PSDs with axial distance from nozzle throat at different radii.

3.2 3D Heat Flux Validation

3.2.1 Mapping

The mapping of the IR data to the solution domain was perhaps the most crucial step in the 3D solution. Overly specific maps were found to dramatically increase computation time, while insufficient detail led to spatial warping of the solution. Spatial mappings of the IR data to the domain were compared to CFD results for verification. While the heat flux magnitudes from the CFD have not been verified, the geometry is exact, and the geometry-related features shown in Figure 3.6 were used to validate mapping.

The earliest attempts at mapping were created by identifying which pixels aligned with the exterior of the fins, their corners, and the forward-most visible points. Figure 3.7 shows relatively good mapping performance, although spatial warping of the vortex heating streaks is clear. The

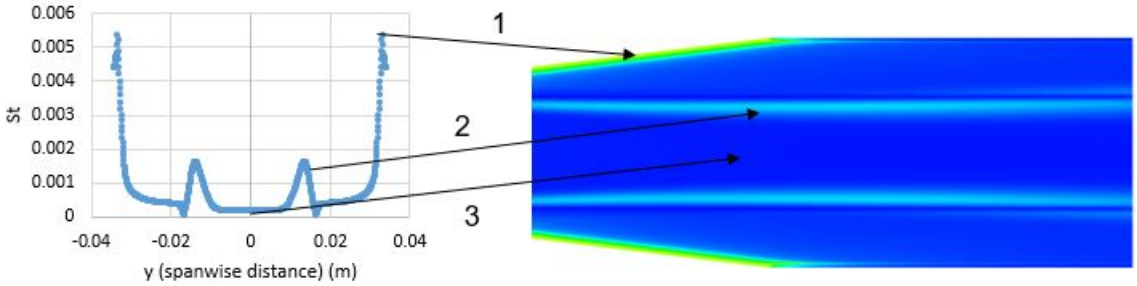

Figure 3.6: Geometry alignment features: 1 - fin- leading edge heating peak, 2 - horseshoe vortex heating next to corner (cold), 3 - cylindrical body laminar heating.

backsides of the fins were symmetric with the top side, as designed. Improvements were made to the scaling images taken, with a focus on placing points around each feature, not just around the entire visible portion of the model.

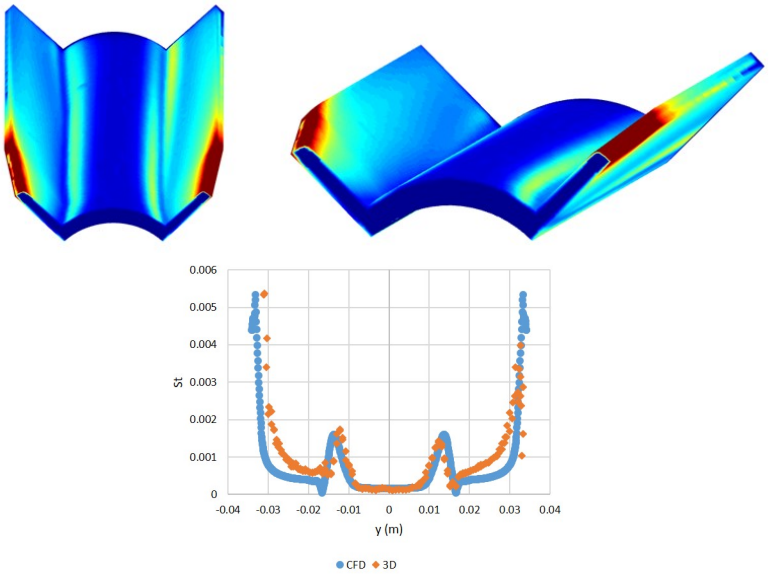

Figure 3.7: Heat mapping onto 3D domain using exterior points, ACE run 4490.

Each map was made in a detailed, user-involved process, which led to variability in the certainty of mapping from run to run. Regardless, the improved scaling shots were shown to dramatically improve map performance, as detailed in Figure 3.8. The following map is representative of im-

proved mapping performance. The hot spikes due to leading edge heating exactly aligned with the CFD, as generally did the vortices as well, although the vortices were not expected to perfectly align. The mapping of the cold corners between the cylinder and the fins was not perfect, but was within one maximum node spacing of the correct location.

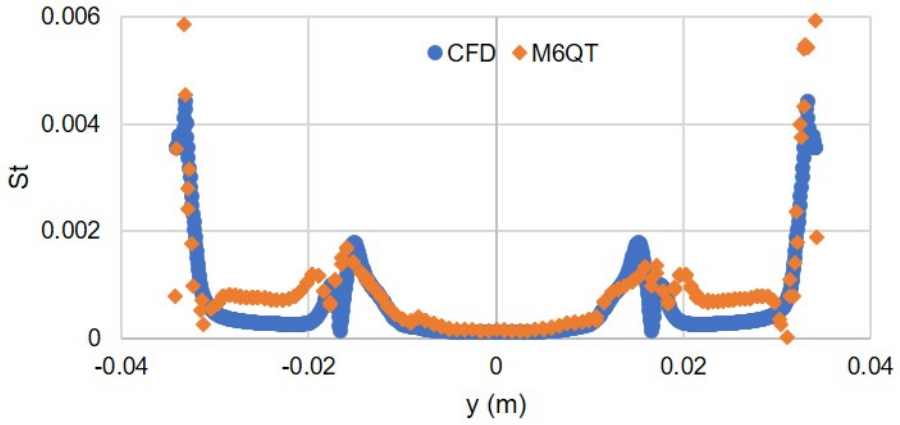

Figure 3.8: Improved mapping, ogive, 4-fin, $Re/m = 10 \times 10^6$, x = 0.4 m.

3.2.2 Grid Convergence

As with any numerical method, the solution must be independent of the mesh. For this, data collected on the 4-fin section from run 4640 were reduced using two meshes with a maximum spacing between nodes of 2.0 mm and 1.5 mm respectively, shown in Figure 3.9. As shown in Figure 3.10, the RMS of heat flux was converged within 2.8%, which shows the solution had converged over the vast majority of the domain. Heat flux at the peaks, caused by either of the top corners, only converged within 7%, accounting for almost all of the discrepancy. The issue was simply having enough grid points to resolve those structures. Denser meshes (max spacing of 1 mm) were problematic due to memory constraints. The MATLAB function was limited to a single core for processing, restricting the size of the domain. Development of a code that could partition

the domain was left as potential future work should it become necessary. For this work, meshes generated with a maximum spacing of 2.0 mm were deemed sufficient.

Figure 3.9: Meshes for convergence study, 2mm (top) and 1.5 mm (bottom) max node spacing.

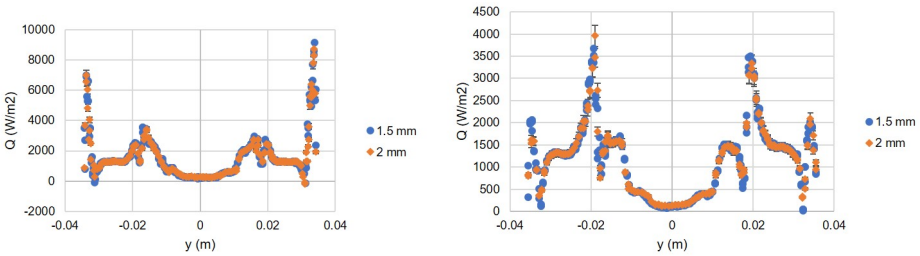

Figure 3.10: Grid convergence at x = 0.40 m and x = 0.45 m (left to right).

3.2.3 Comparison to other methods

The 3D heat flux reduction method was compared to the 1D method and CFD in Figure 3.11. Performance was identical between all three methods on the cylindrical part of the body, as expected. Here, the 1D assumptions should have been quite good and the CFD was validated for these conditions. The benefits of the 3D method became more apparent in the 3D regions of the flow, with the 3D method giving about 50% lower heat flux values on the fins than the 1D method.

Additionally, the 3D heat flux was mapped better and the solution accounted for lateral conduction, matching peaks and troughs more accurately in the spanwise direction. Mapping was built into the 3D solution method, whereas the 1D solution required significant post-processing to achieve the same mapping fidelity.

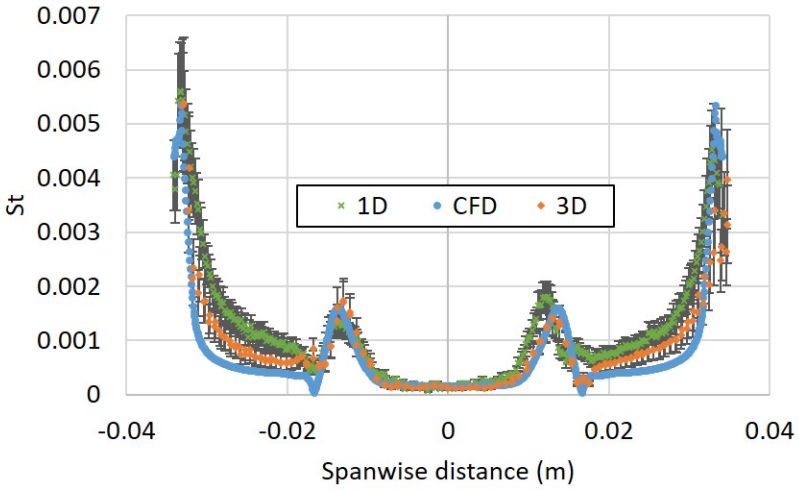

Figure 3.11: Comparison of data reduction methods for run 4492, ogive, 4-fin model, $Re/m = 5 \times 10^6$, x = 0.4 m.

3.3 Fin Cone

The fin-cone was the first model printed using improvements based upon the multi-fin blockage models. Both heat flux and surface pressure were measured and compared to results from other experiments and computations on the same geometries to validate the manufacturing and data reduction methods.

3.3.1 ACE

For run 4883, the fin was oriented vertically with respect to the camera, allowing the camera to see the conical surface on both sides of the fin. Because the heating was only on the cone surface, it was appropriate to use the 1D heat flux reduction tool. IR temperature data in Figure 3.12 showed remarkable symmetry across the fin, which indicated that the model alignment was straight and the

nose-tip to body joint was symmetric. It also reveals that the pressure sensors were placed exactly where they were desired to be between the two heating streaks. Transition to turbulence and vortex breakdown were observed, most noticeably starting at unit Reynolds numbers of $5 \times 10^6 m^{-1}$. Transition at this low of a unit Reynolds number could be expected due to the noise environment of the ACE tunnel.

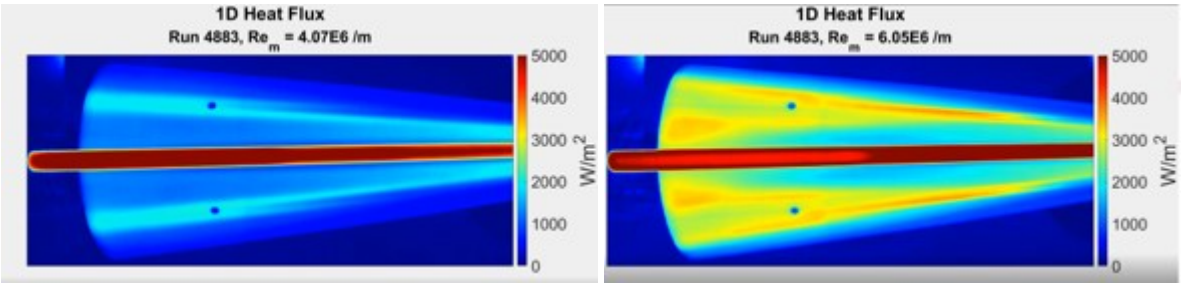

Figure 3.12: 1D Heat Flux of the fin-cone in ACE at $Re/m = 4 \times 10^6$ & 6×10^6, flow is right to left. The view is directly onto the fin, with the hot leading edge in center of image.

Pressure frequency spectra were extracted from the PCB 132B38 pressure measurements, shown in Figure 3.13. They showed symmetry of the model by having the same peak frequency of 130 kHz, if not the same power, at $Re/m = 3 \times 10^6$. This frequency may have been related to the vortex, being about 50 kHz lower than the vortex frequency measured at $Re/m = 7 \times 10^6$ by Turbeville [19]. The pressure frequency spectra completely faded into turbulence by the time the tunnel hit $Re/m = 4 \times 10^6$, which shortly preceded noticeable vortex breakdown in the heat flux maps. While ACE was a conventional facility, it was known to have a significant rise in freestream noise levels at $Re/m = 3 \times 10^6$, which may have been the cause of the change in pressure spectra under the vortices [31].

During run 4881, the fin was oriented at a 45° angle with respect to the camera, allowing the temperature to be measured on the fin surface. The 3D heat flux tool was used to reduce the data across all visible parts of the model. Traces of heat flux were plotted 0.33 m and 0.35 m from the nose, to match the location of the PCB and the location of heat flux in the M6QT respectively.

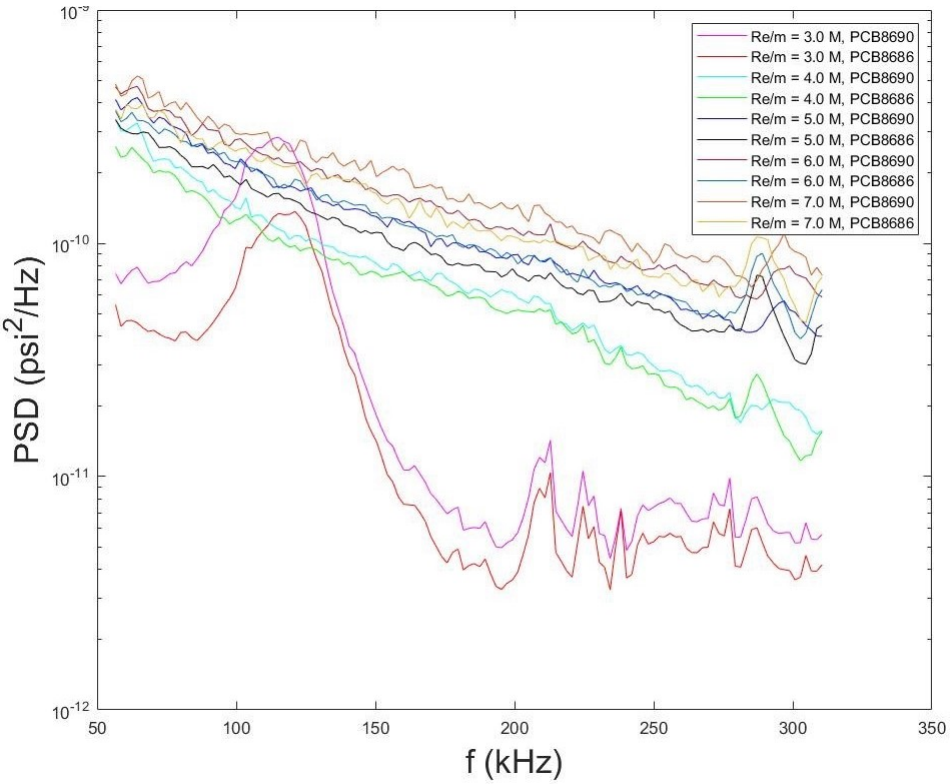

Figure 3.13: PSD during a unit Reynolds number sweep of the fin-cone in ACE, run 4883.

These data were taken concurrently with PCB pressure measurements, leading to a lack of heat flux data on the PCB itself, shown by the gap between 30° and 32° at x = 0.33 m. A schematic of the visible features and coordinates is shown in Figure 3.14.

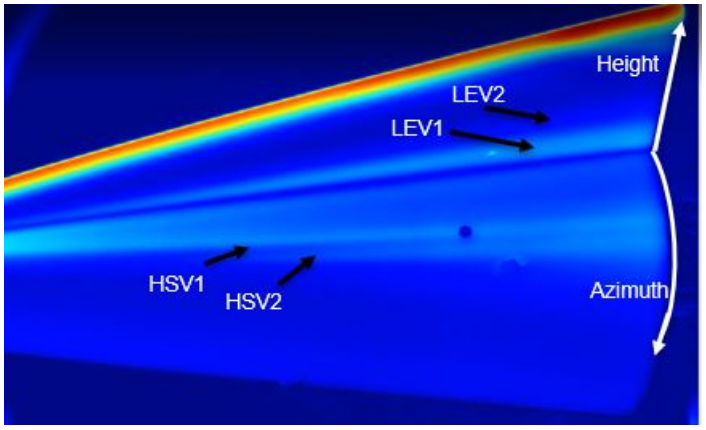

Figure 3.14: View of Fin-cone at 45° showing primary and secondary leading edge (LEV1 & LEV2) and horseshoe (HSV1 & HSV2) vortices, and the coordinate system for heat flux trace extraction.

Heat flux traces are shown in Figure 3.15 both on the body and the fin. On the cone, the trace at $Re/m = 3 \times 10^6$ showed only one real peak, corresponding to the primary horseshoe vortex, approximately 28° away from the fin. On either side of this peak, the heat flux took on a flat shape at both locations, likely the laminar heating rate. However, this heating rate was higher between the fin and the streak, which was also measured by Turbeville in quiet flow [19]. Computational analysis found that the horseshoe vortex structure altered the height of the boundary layer, which would account for the different heating rates measured in these experiments as well as the most unstable frequencies [22]. As unit Reynolds number increased, heat flux increased across all points on the conical body and the primary vortex seemed to move away from the fin. The secondary horseshoe vortex formed at $Re/m = 4 \times 10^6$ and eventually achieved higher heating rates than the primary vortex. However, the largest increase in heating was due to vortex breakdown. This breakdown was indicated by turbulent heating levels across a broad swath of the cone at $Re/m = 6 \times 10^6$, rather than heating in confined peaks. As the heating peak was broadened, the peak heating rate decreased, leading to a lower peak heating rate at x = 0.35 m than at 0.33 m. These trends were what could be expected at a much lower unit Reynolds number in a conventional tunnel, compared to the lack of breakdown in a quiet tunnel.

Heating on the fin was primarily due to two features, with the leading edge vortex close to the

cone surface and leading edge heating far from the surface. The data was truncated to show only the flat face of the fin, due to leading edge heating dominating the heat flux due to vortices. The leading edge vortex remained in a fairly constant location, or any effect on location was below the resolution of the grid, although the heating level was quite sensitive to unit Reynolds number. For $Re/m = 5 \times 10^6$ and below, the heat traces eventually converged to the same heating level on the middle of the fin, which then increased to the leading edge value of each case. At $Re/m = 6 \times 10^6$, the vortex heating rate almost doubled compared to the next lowest case. It appeared that the vortex had not broken down, due to the peak heating at x = 0.35 m being in roughly the same location and at a higher level than at x = 0.33 m. However, at both locations and all conditions, peak heating due to the leading edge vortex system was about the same as peak heating due to the horseshoe vortex system.

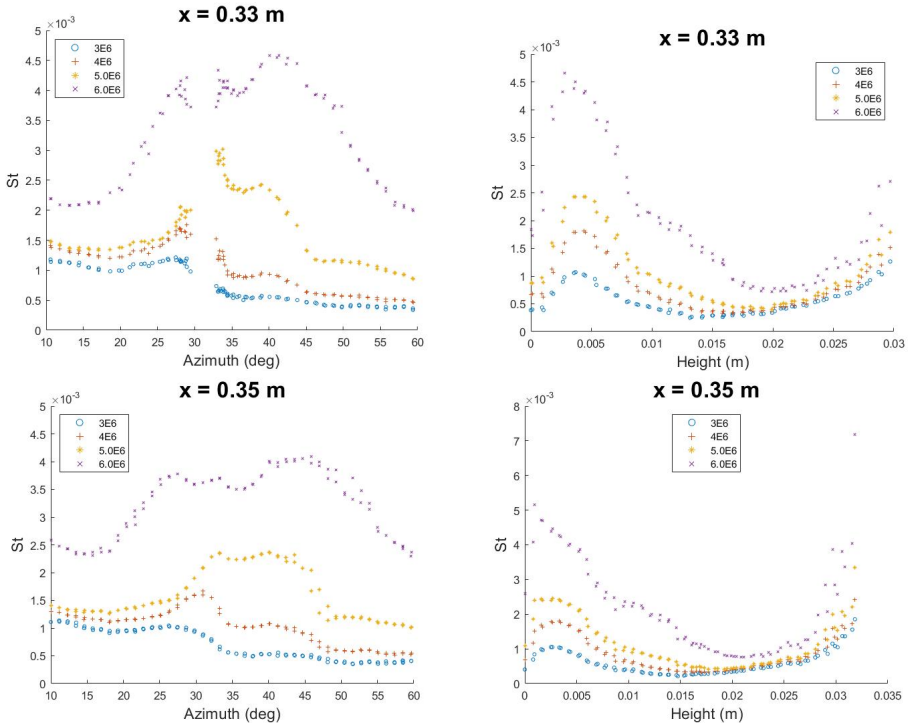

Figure 3.15: Heat flux traces for several unit Reynolds numbers in ACE on the fin-cone. Heat flux on the cone is plotted against azimuthal distance (left) while heat flux on the fin is plotted against height above the cone surface (right).

3.3.2 M6QT

The ACE fin-cone experiments were repeated in the M6QT at higher unit Reynolds numbers, although the visible portion of the model in the IR data was significantly reduced, due to moving the model forward to avoid the compression shock that occurs as the nozzle flow enters the free-jet test section. The M6QT data could best be used to compare results to CFD and experiments in other quiet facilities.

Heat flux traces, shown in Figure 3.16, were extracted at x = 0.35 m, 2 cm behind the PCBs, due to the PCBs being too far forward to be viewed by the IR camera. The heat flux on the cone showed two peaks at approximately 31° and 36°, although the inner, primary horseshoe vortex widened and moved towards the fin at higher unit Reynolds numbers. This corresponded well with the results found by Turbeville, who found streaks at approximately 30° and 36°, with the outboard vortex having higher heating at higher unit Reynolds numbers and further back on the model [19].

Two peaks were shown on the fin at well, corresponding to the primary and secondary leading edge vortices. It confirmed that secondary vortices were generated at higher unit Reynolds numbers, regardless of tunnel freestream noise. It appeared that both were pushed away from the conical body as unit Reynolds number increased. However, peak heating of the primary vortex remained consistently at 4 mm above the cone, while the secondary vortex peak moved up the fin at 1 mm/million (Re/m). Comparing peak heat flux values showed that all vortex heating increased with unit Reynolds number until St = 0.003, which occurs for the secondary (outboard) horseshoe vortex at all three conditions and the primary leading edge vortex for $Re/m = 8.0 \times 10^6$.

Pressure spectra were also taken in the M6QT and shown in Figure 3.17. Unlike in ACE, quiet flow allowed non-turbulent spectra to be measured at Re/m = 7.0 and 7.5 $\times 10^6$. Run 4924 showed symmetric frequencies on both sides of the fin at $Re/m = 7.0 \times 10^6$ with peaks shown at 170 and 235 kHz. However, alignment might have been slightly off as 235 kHz is a little low for the expected 2nd mode. This misalignment was confirmed as turning the fin to 45° with respect to the camera in run 4934 led to the measurement of a vortex frequency on one PCB and the 2nd mode on the other. Slight misalignment would affect vortex location which in turn affects which

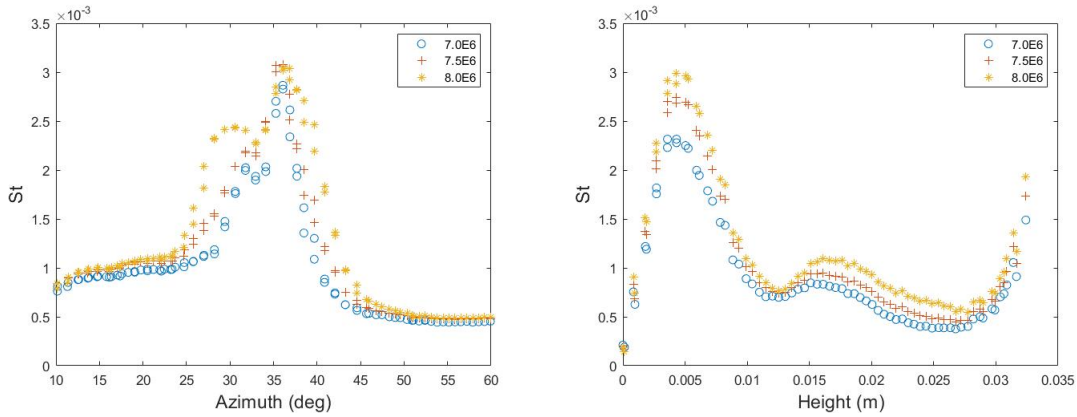

Figure 3.16: Heat flux traces at increasing unit Reynolds number on the fin-cone in M6QT, x = 0.35 m, conical body (left) and fin (right).

modes are seen by the sensor [19]. Additionally, the 2nd mode was highly sensitive to an AoA even without the presence of a fin [25]. Perfect alignment was not deemed necessary to say that model manufacturing was adequate to study transition modes. At $Re/m = 7.0 \times 10^6$, a 180 kHz frequency disturbance was captured by one PCB while the opposite side captured a 270 kHz frequency. This closely matched the 180 kHz vortical mode and 280 kHz 2nd mode frequencies observed at Purdue on the same geometry at these conditions [19]. Both of these frequencies were washed out by $Re/m = 8.0 \times 10^6$. Not only was the new 3D printing manufacturing reliable enough to symmetrically align the vortices from the SBLI, but it allowed the replication of the same frequencies as measured by stainless steel and PEEK machined models.

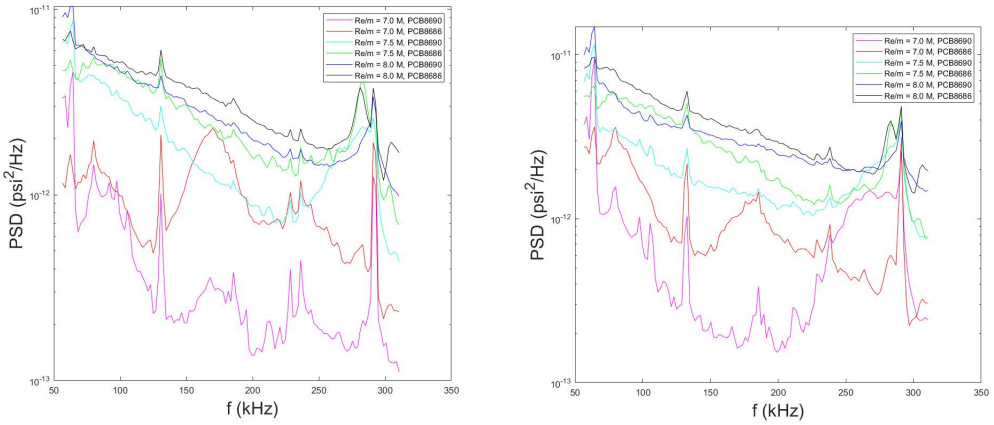

Figure 3.17: PSD at increasing unit Reynolds number on the fin-cone in M6QT, run 4924 (left) and run 4934 (right).

3.4 4-Fin Configurations

The multi-fin configurations will be used for a parametric study of models with multiple SBLI. Although both 3-fin and 4-fin blockage models were initially available, the 4-fin models were prioritized to facilitate collaboration with computation partners. The majority of the work presented in this thesis provides a basis for further study, using blockage models to outline the parameter space of the study and validate the tools and methods needed for further investigation. Model alignment studies were conducted to quantify the uncertainty of results with the blockage models as well as inform alignment of future models. Differences between ACE and the M6QT were considered and anomalous behaviors were reported. Finally, the parameters of fore-body geometry and units Reynolds number were briefly explored.

3.4.1 Model Alignment Sensitivity

It has generally been shown that SBLI are extremely sensitive to changes in alignment with the oncoming flow [26, 19]. Collaboration with computational partners quickly revealed that validation requires model fidelity and alignment that could not be achieved with tunnel blockage models. As part of the initial survey of the multi-fin models, the effects of small changes in model alignment were measured to first explain any discrepancies between CFD and experiments and also

inform later experiments to check model alignment. For both tunnels, the view of the model was chosen such that two fins at 45° or 60° with respect to the optical axis of the camera were visible. Both models were viewed from the top of the tunnel, with positive AoA being defined as the nose moving towards the top of the tunnel (out of the page), and positive yaw being defined as the nose of the vehicle to the right (towards the top of the picture). Unlike the fin-cone geometry, where the leading-edge vortex system stayed on the fin and the horseshoe vortex stayed on the conical body, the horseshoe vortices on the multi-fin geometries tended to cross over from the cylinder body to the fins. This made the between-fin view the most advantageous for observing the entire flow field and decided the orientation of the axes which define AoA and yaw.

The full, 3D heat flux solution was used to analyze the alignment sensitivity data. This automatically mapped the data to the correct 3D coordinates for comparison to CFD and kept the data processing similar for all results. However, the heat flux results on the fins were calculated assuming symmetric heating on both sides of the fin. Data would need to be simultaneously measured on both sides of the fins for certainty of the heat flux values, but only one camera was used.

3.4.1.1 ACE: Alignment Sensitivity

The alignment sensitivity study in ACE was the only study conducted using the improved models, with the straight nose-body and the 4-fin aft-body. The junction between the adapter piece and the model was purposely designed to join together both faces that had the 3D printing support material connections. Shimming was required to align the spar and adapter to the model correctly, giving the reference alignment. A 0.01" shim was then placed in between the adapter piece and the rear of the model to create a deviation of 0.5° in the desired direction. However, the imperfection of the model, as well as the sensitivity of the alignment to the torque of the screws, made perfect alignment impossible. The actual alignment achieved is reported in Table 3.1.

The results of the alignment sweep in ACE show a much larger sensitivity to yaw than to AoA, a key distinction from the M6QT results. Heat flux maps, shown in Figure 3.18, give a view of the overall structure of the flowfield. Flow is from left to right. The portion of the model visible to the IR camera was shown with the non-dimensional heat flux placed where the corresponding pixels

Run Number	ΔAoA°	ΔYaw°
4943	0.00	0.00
4944	0.05	0.54
4945	0.00	-0.34
4946	0.42	0.08
4947	-0.30	0.03

Table 3.1: Model alignment variation for sensitivity study ($\pm 0.10^{\circ}$).

were. Positive yaw corresponded to the nose of the model moving toward the top of the page. This caused the visible side of the lower fin to be hidden from the oncoming flow, while the visible side of the upper fin was the compression surface of the fin. The resultant pressure gradient drove both horseshoe vortices from the top fin toward the lower. The heat streak that crossed over from the cylinder to the fin first experienced higher heat flux along its path in all three cases.

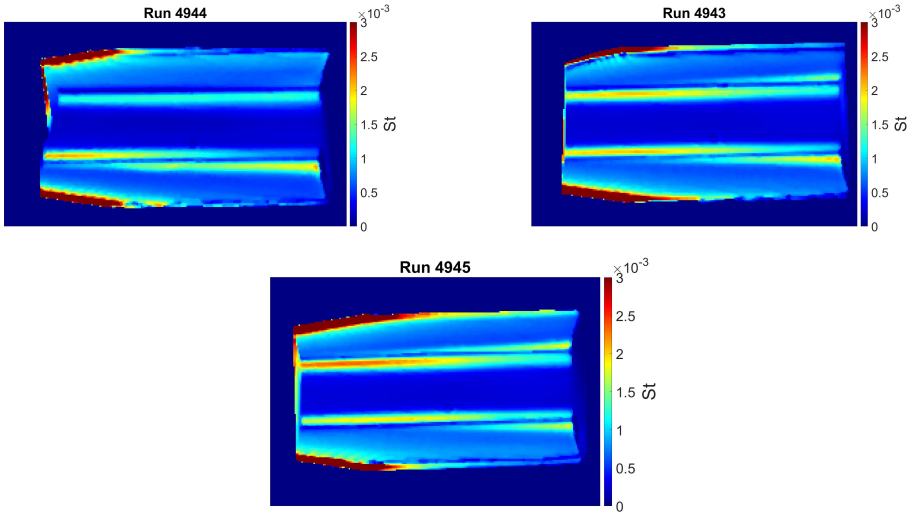

Figure 3.18: Heat flux maps for $\Delta Yaw = 0.54^{\circ}, 0.0^{\circ}$, and -0.34° at $Re/m = 5 \times 10^6$, improved, straight, 4-fin model in ACE.

Finally, traces of heat flux were extracted normal to the axial direction at three locations on the fin section of the body and compared across the yaw sweep and against CFD in Figure 3.19. There was very little variation at the foremost location. As seen in the heat flux map, the vortex

that moved from the cylinder to the body has a higher heat flux, even at this forward location. The peak heating at the leading edge of the fin did not have great agreement. However, this location was most sensitive to grid refinement for both the experiment and the CFD. Moving to the mid-fin location, it could be seen that heat flux on the cylinder excellently agreed with CFD, especially in the reference case. Heat flux on the fins was much higher for the 3D heat flux method than for the CFD, especially where the vortex heating had crossed over to the fin. This trend remained true in all cases, as will be seen in the other studies.

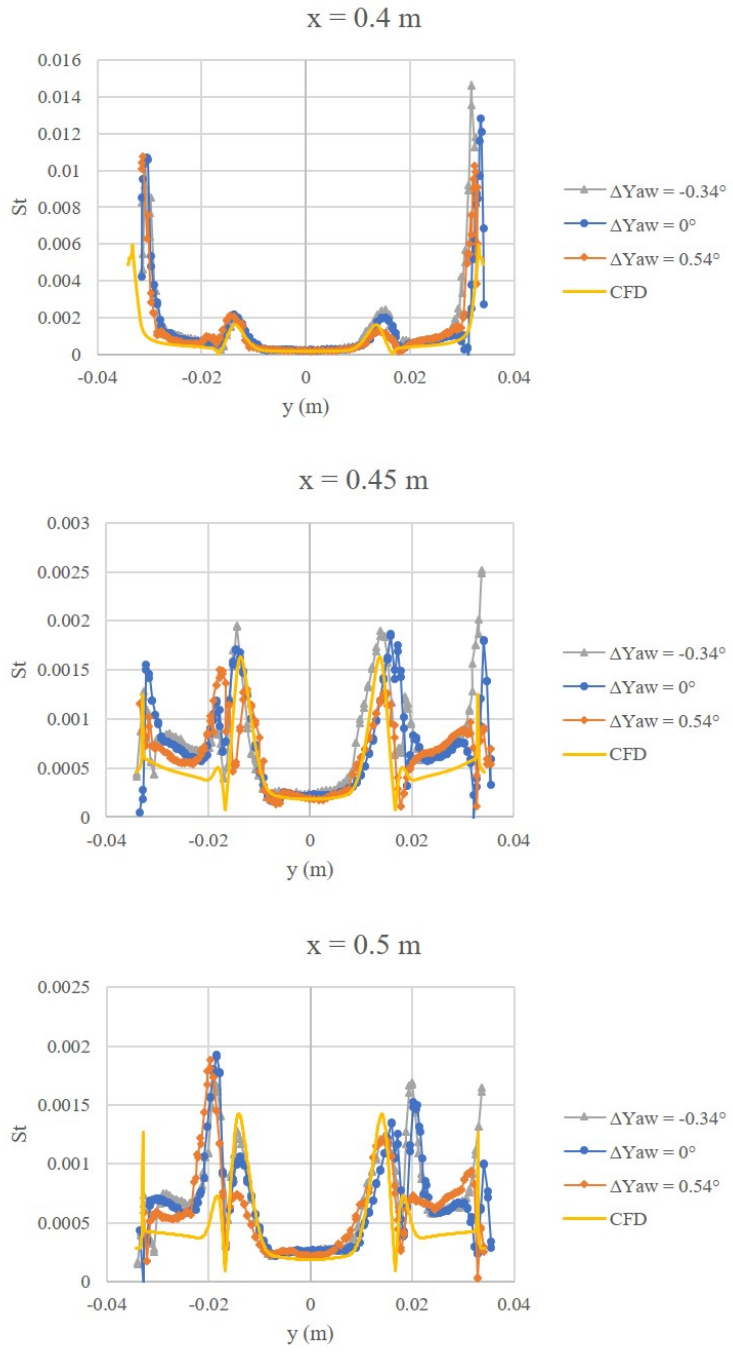

Figure 3.19: Yaw sweep at $Re/m = 5 \times 10^6$, straight, 4-fin model in ACE, (CFD from private correspondence with Travis S. Kocian, TAMU, 2021).

3.4.1.2 M6QT: AoA Sweep

Alignment sensitivity in the M6QT was conducted before the printing of the improved models. Due to the design of the models and the sting in the test section, yaw was fixed and AoA was varied, meaning the nose was moved up or down relative to the floor of the test section by placing shims at the base of the sting. Something similar to a yaw study could be achieved by moving the IR camera to the side window and sweeping through the same AoA alignments. During the study, the screws of the sting cap were tightened with a torque wrench to ensure that the sting-spar alignment was the same every time. The AoA sweep in M6QT was conducted on the ogive nose-body and 4-fin aft-body at $Re/m = 10 \times 10^6$ for comparison of data with CFD results.

The sweep viewed from the top showed a change in the number of features present with small changes in AoA, as seen in Figure 3.20. The positive AoA indicated the nose is angled up with respect to the tunnel floor, meaning the visible, top side was the suction side of the model. At positive AoA, the horseshoe vortex heating streak moved almost entirely onto the fin. It appeared that secondary vortices formed and ran parallel to the corner on the cylinder body, with two distinct streaks appearing at AoA = 1° on at least one side of the cylinder. As the AoA became more negative, the horseshoe vortex remained more and more on the cylindrical body. Additionally, a new heating streak was formed on the fin, about halfway up from the cylinder. This streak appeared to transition to turbulence on the very corners of the fin at AoA = -1°. This feature did not appear with a change in AoA in ACE, which indicates that it was also dependent on units Reynolds number.

Comparison to the fin-cone helped explain some of the general flow features. On the fin-cone, a horseshoe vortex was formed on the body while a leading-edge vortex was formed on the fin [19]. The negative AoA cases were similar to the fin-cone as the cylindrical body became a compression face, creating a pressure gradient and crossflow pattern right at the beginning of the fin. This mechanism was outlined in detail for the fin-cone [17]. The pressure gradients that shaped the horseshoe vortex paths were created by compression or expansion happening on the fin faces themselves, rather than on the cylinder body. As the AoA became more positive, expansion of the

flow over the fins seemed to suck the horseshoe vortices onto the fin faces, while compression at negative AoA pushed them onto the cylinder body. Unlike the fin-cone, the path of the horseshoe vortex was much closer to the fin on the 4-fin model, likely due to the presence of another fin only $90°$ away. Additionally, the primary vortices did not as easily produce secondary vortices, which only appeared to happen when the horseshoe vortex crossed over to the fin.

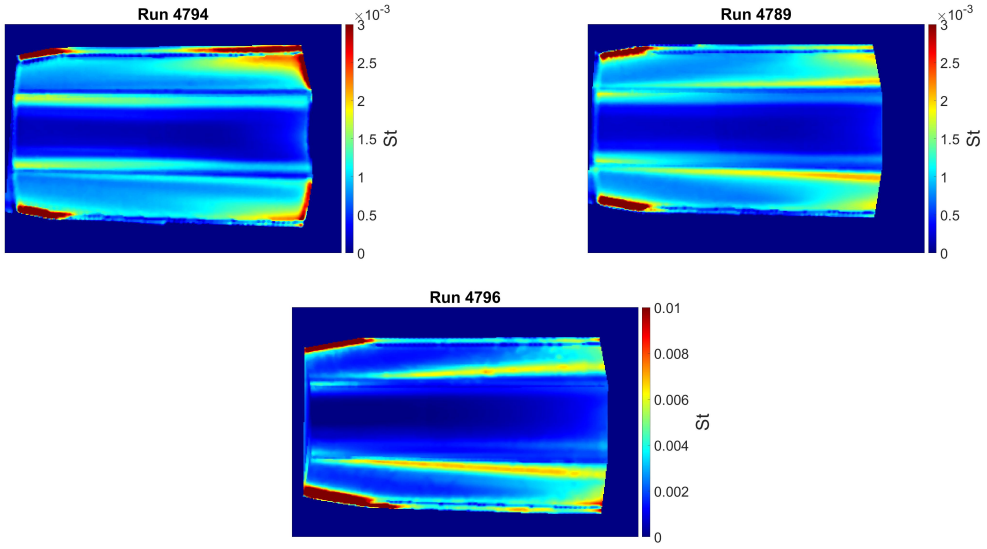

Figure 3.20: Heat flux maps for $\Delta AoA = -1°, 0°$, and $1°$ at $Re/m = 10 \times 10^6$, ogive, 4-fin model in M6QT.

Traces of heat flux were extracted normal to the axial direction at three locations on the fin section of the body and compared across the AoA sweep and against CFD in Figure 3.21. Excellent agreement was achieved between all cases and CFD for laminar heating on the cylinder body, with the exception of the highest angle of attack. Specifically the reference case, $\Delta AoA = 0°$, achieved agreement within 11% with CFD on the cylinder body at the two upstream locations, including the heating due to the horseshoe vortices. Experiments confirmed the CFD prediction that the primary heating peak of the horseshoe vortex crosses over to the fin. Additionally, the CFD showed a waviness in the profile of the horseshoe vortex on the cylinder that intensified as

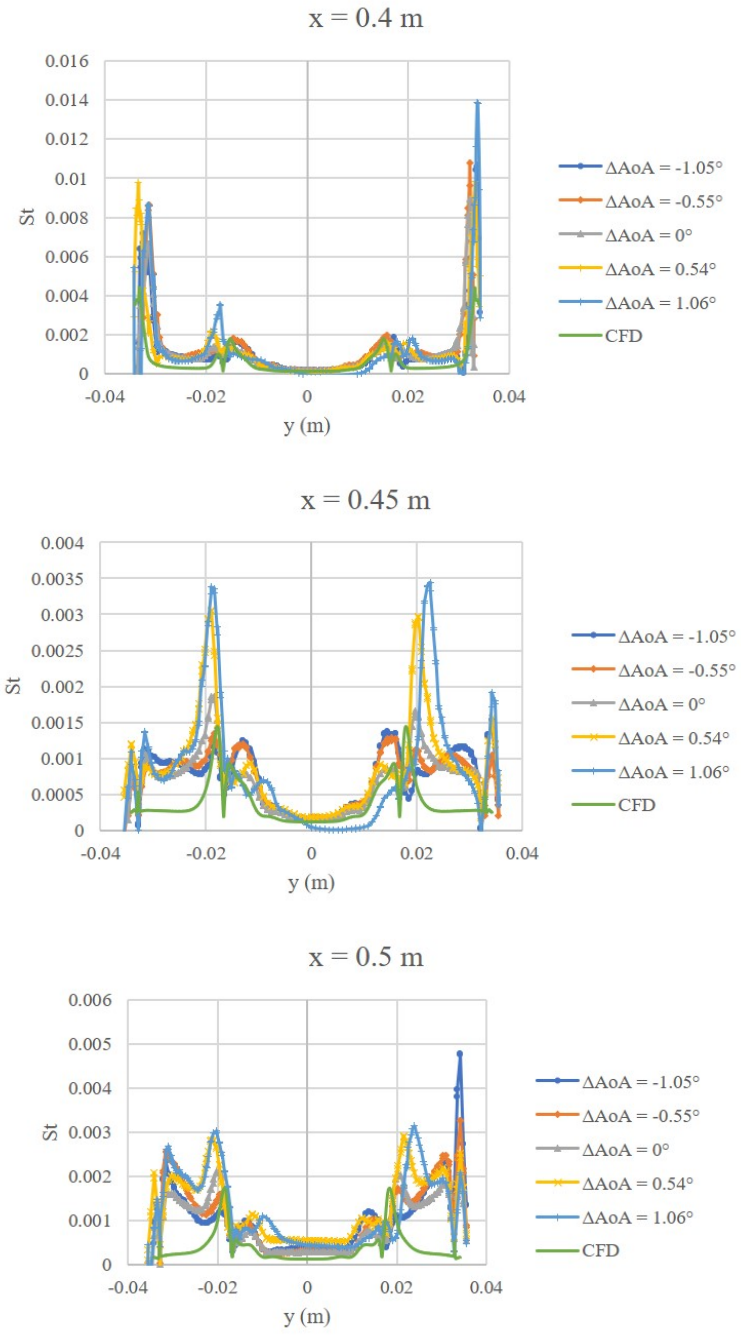

Figure 3.21: AoA effects at $Re/m = 10 \times 10^6$, ogive, 4-fin model in M6QT, (CFD from private correspondence with Travis S. Kocian, TAMU, 2021).

the vortex crossed over to the fin, perhaps corresponding to the development of secondary vortices, which was captured in the experiments, although they were most distinct at positive AoA.

Many discrepancies were found between the different AoA and CFD. Experimental heat flux on the leading edge was 2-3 times the value predicted by CFD. Again, this was likely more due to the refinement of the domain mesh than any physical cause. Heating on the fins was, without exception, higher in the experiments than in the CFD. Looking particularly at the x = 0.45 m case, the negative angles of attack developed a heating peak on the outboard part of the fin, due to a leading edge vortex. These same AoA showed an increase in heating by 50% on the cylinder due to the horseshoe vortex. At positive AoA, the horseshoe vortex caused a dominant peak to appear on the fin near the corner. It seemed that the CFD does not indicate any heating peak on the fin besides that caused by the horseshoe vortex. Based on the agreement on the cylinder, this discrepancy must be related to differences on the fins. The first possibility is that higher heating on the backside of the fin caused an apparent increase in heating on the visible side of the fin. This was confirmed by the transition anomaly, as shown in the next section. The second possibility is that the freestream noise caused growth of instabilities on the fin that led to higher heating levels. The final possibility is that numerical error was introduced due to strong gradients from the vortex streaks and sparseness of node points throughout the fin, as was shown to be possible in previous comparisons of numerical methods [35]. More work will need to be done to distinguish between these possibilities.

3.4.2 M6QT Transition Anomaly

Figure 3.22 shows remarkable similarity between ACE and M6QT. This indicated that data from the two tunnels can be conglomerated to reach a larger range of unit Reynolds numbers, rather than simply finding the differences between the two tunnels. However, experiments at $Re/m = 10 \times 10^6$, shown in Figure 3.23, revealed some differences that may confound the attempt to compare data between the two facilities.

Due to the constraints of working in the M6QT, the effects of yaw were studied by positioning the IR camera in the side window, but the study was foiled as entirely anomalous behavior was

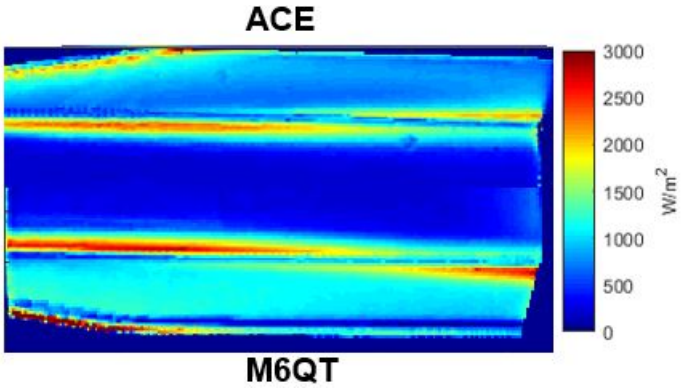

Figure 3.22: Comparison of ACE and M6QT results, ogive, 4-fin model, $Re/m = 7.5 \times 10^6$.

observed. Clearly shown in the ΔT contour below, transition to turbulence occurred on the top fin with total temperature changes of 30-40 K in 10-15 seconds. For reference, laminar flows typically see 3-4 K in the same amount of time. This data could not be converted into heat flux due to the asymmetry of the heating on either side of the fin and invalidates the heat flux estimates on the fins for all top-view runs in the M6QT. The results on the fin should be considered qualitative. Transition also seemed to occur on the cylinder body, with a receding transition front from the top of the model to the bottom. Additionally, the only heating streak observed existed entirely on the fin, indicating it is the leading edge vortex, although it could have been the horseshoe vortex after having crossed over incredibly far forward on the model.

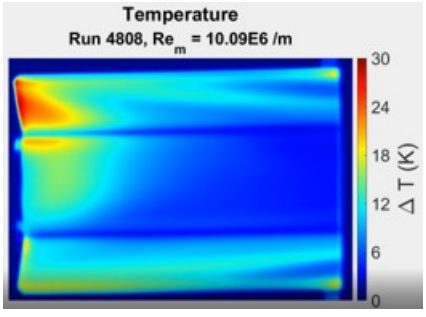

Figure 3.23: Transition on top fin viewed from side window with flow right to left on the ogive, 4-fin model at $Re/m = 10 \times 10^6$ in M6QT.

The cause of the asymmetric transition will be a point of future research. This asymmetry was observed to persist after looking through the top and both side windows and was determined to be independent of the model by varying the alignment of the model bodies as well as the specific side viewed by the IR camera. The general structure of the heating profile did not change with yaw, as viewed from the side window, although there was some variation in the intensity and location of heating. This indicated that the anomaly was caused by a feature of the freestream, but the characterization of the M6QT found that the tunnel was still performing as initially characterized by Dr. Hofferth in 2010 [28, 38]. There was no correlated asymmetry in the freestream noise levels, which were almost entirely axisymmetric. There was a slight asymmetry in Mach number, with the left and right side of the nozzles decelerating more than the top, but only by approximately Mach 0.06, or 1%, at the exit plane. Asymmetries in Mach number are likely due to asymmetries in the boundary layer, which causes discrepancies between the viscous and inviscid Mach numbers of the tunnel. It is known that the temperature profile of the nozzle was not perfectly symmetric, but variations have never been significant enough to cause any anomalies on other models. The characterization did show that the majority of the fin section was exposed to non-quiet noise levels at $Re/m = 10 \times 10^6$. Additionally, analysis of the spectral content of the noise indicated that the tunnel boundary layer was radiating a disturbance at 140 kHz in those regions of significant noise. Although that frequency should be altered somewhat by the process of receptivity into the model boundary layer, it is close to the most amplified frequency of 165 kHz predicted by stability analysis at the transition location (private correspondence with Travis S. Kocian, TAMU, 2021). The noise level and frequency would not explain the asymmetric transition, on the bottom side of the top fins and the sides of the cylinder. Ultimately, the transition of the freestream from a quiet core to the noisy, free-jet test section impinged upon the complex SBLI and may make IR measurements on the multi-fin models impractical in the M6QT.

3.4.3 Effects of Fore-body Geometry

The effects of fore-body geometry were measured and compared to CFD in Figure 3.24. The data at $Re/m = 5 \times 10^6$ was collected in ACE, during the initial campaign using the blockage

models. The unit Reynolds number was swept from $2 - 7 \times 10^6 m^{-1}$ with the data extracted from the frames when $Re/m = 5 \times 10^6$. The data presented from the M6QT was averaged over the last 5 seconds of one run, where the unit Reynolds number was held at 10×10^6, and from another run where the condition was held at $Re/m = 10 \times 10^6$. As shown in the alignment studies, the CFD matches the experiments on the cylinder body, with the exception of the peaks of the vortices. This has been attributed to a lack of nodes at those points and not any error of the method. However, the heating on the fins differs by 50% or more in the $Re/m = 5 \times 10^6$ case and up to 4 times the value in the $Re/m = 10 \times 10^6$ case. Regardless, the difference between fore-bodies is negligible with all other factors held constant. The only exception is the experimental results at $Re/m = 10 \times 10^6$, but the AoA sweep showed that a change of 0.5° could result in similar differences. The change of the angle due to the joint between the different fore-bodies with the 4-fin section could account for this error. Therefore, no significant difference between the two fore-bodies or the pressure gradients in the oncoming boundary layer could be claimed.

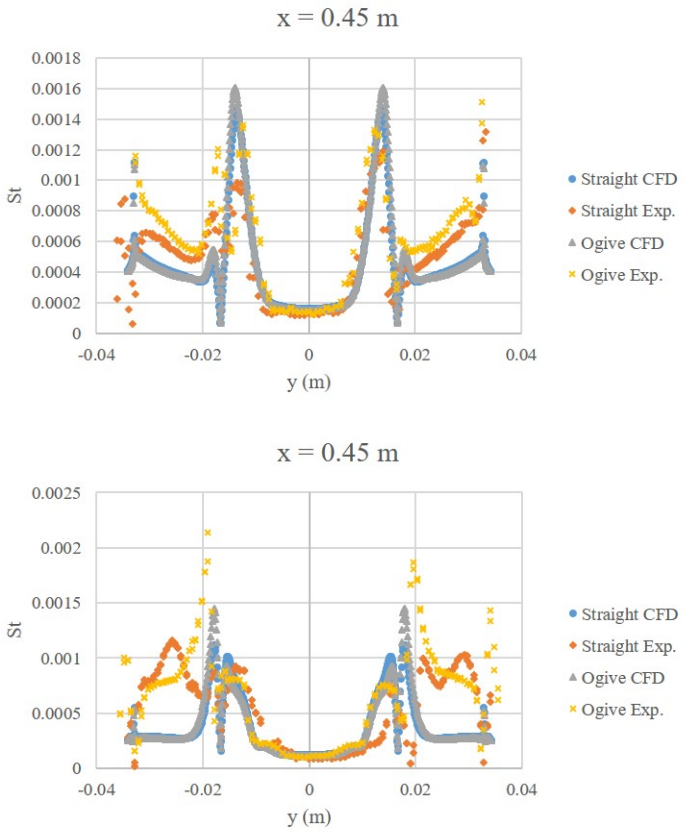

Figure 3.24: Comparison of the straight and ogive forebodies at $Re/m = 5 \times 10^6$ in ACE (top) and $Re/m = 10 \times 10^6$ in M6QT (bottom), (CFD from private correspondence with Travis S. Kocian, TAMU, 2021).

3.4.4 Effects of Unit Reynolds Number

Because of the long duration of the tunnel run time, a constant ramp of unit Reynolds number of the freestream from roughly $2.0 - 7.0 \times 10^6 m^{-1}$ in ACE and $7.5 - 11.5 \times 10^6 m^{-1}$ in M6QT can be conducted while holding as steady of a condition as can be achieved in other facilities. The tunnels could also both be run at constant unit Reynolds number and achieve a steady heat flux solution within 4-5 seconds of achieving run conditions, giving more certainty of the flow conditions as well as facilitating quicker turn around between experiments. These runs were used for rapid comparison of geometries or alignments. For the study of the effects of unit Reynolds number, however, one sweep in ACE and one in the M6QT were compared. The two runs are

plotted separately due to key differences between the experiments. Both are conducted on the same model, using the ogive fore-body and the 4 fin section. Together, the two runs cover the range of $Re/m = 2 - 11.5 \times 10^6$. Run 4492 in ACE was part of the very first campaign with the blockage models and used the former mapping methods, leading to some compression of the total span of the model, while run 4641 in M6QT was conducted months later using the improved mapping methods. The reference alignment in ACE is known to have an approximately 0.25° yaw, which is shown to cause the horseshoe vortex to cross over more for y < 0, while the M6QT data is much more symmetric. Additionally, the ACE experiments tend to have higher freestream noise levels as well lower wall temperatures due to radiative heating from the nozzle walls during model installation. Both of these effects may lead to higher Stanton numbers. Regardless, useful information on the effects of unit Reynolds number can be extracted from a comparison of these two experiments.

The effects of unit Reynolds number are best shown by comparing traces of heat flux taken 0.45 m from the nose of the vehicle, detailed in Figures 3.25 and 3.26. This is in the straight portion of the fin, behind the leading edge, which dominates the heat flux at the upstream locations. As can be seen in the figures below, the heating increased with increasing unit Reynolds number at all locations. Note, the values further than 0.016 m away from the centerline are on the fin and should be regarded as estimates, particularly for M6QT data due to the known inaccuracy of the fin symmetry assumption. The structure of the flowfield at the lowest unit Reynolds number shows laminar heating rates on the cylinder and the fin, with a heating peak on the cylinder corresponding to the horseshoe vortex. The laminar heating rate is fairly steady at all unit Reynolds numbers. A significant increase in vortex heating is seen in ACE around $Re/m = 4 \times 10^6$. Then, around $Re/m = 6 \times 10^6$, the horseshoe vortex seems to cross over to the fin in ACE. This seems to be reversed in the low unit Reynolds number M6QT data, with cross-over only happening at $Re/m = 8.5 \times 10^6$. This indicated that the noise levels affected the path that the vortices take as well as vortex heating, which is much lower in the M6QT on the cylinder body. Starting at $Re/m = 8.0 \times 10^6$, the structure of the heating pattern showed the development of a new heating streak about halfway

up the fin, corresponding to y $\approx$ 0.028 m, previously referred to as a leading edge vortex in the discussion of AoA. The appearance of this feature only at higher unit Reynolds numbers would explain why the heating pattern was stable for an AoA sweep in ACE, but incredibly sensitive to AoA in the M6QT. It is possible that the appearance of this feature indicates there was a small AoA during run 4641, although it is interesting that the leading edge vortex was dependent on both unit Reynolds number and AoA. The final feature to notice is the appearance of a second, smaller peak on the body, just inside y = 0.01 m, at about $Re/m = 10.5 \times 10^6$. This may indicate a secondary vortex coming off of the horseshoe vortex, as had been seen on models with stronger SBLI [19]. In general, the increase of unit Reynolds number corresponded to an increase in the number of heating peaks or streaks, as well as an increase in heating level.

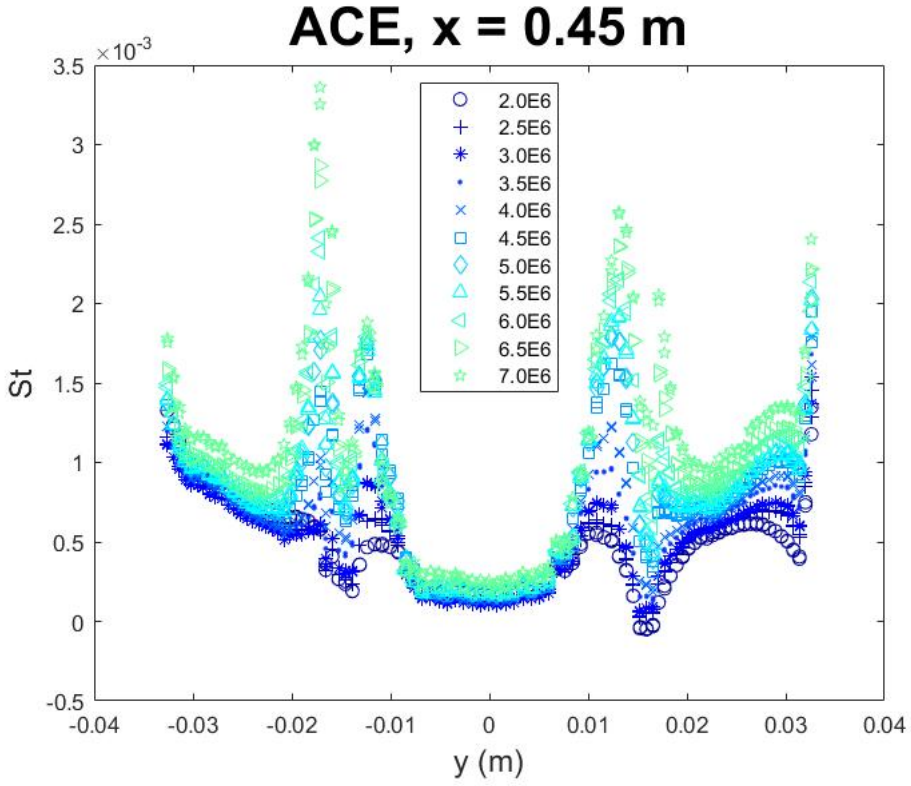

Figure 3.25: Heat flux traces from Run 4492: unit Reynolds number sweep on the ogive, 4-fin model in ACE.

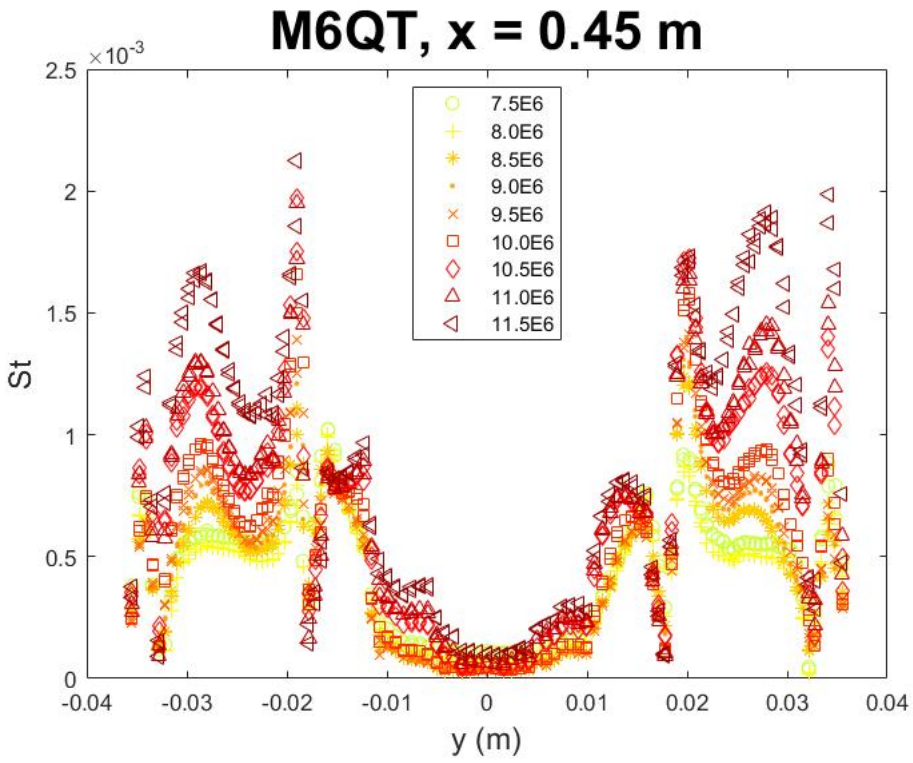

Figure 3.26: Heat flux traces from Run 4641: unit Reynolds number sweep on the ogive, 4-fin model in M6QT.

3.5 3-Fin Models

Investigation of the 3-fin models was limited to testing the basic configurations in both tunnels using the blockage models. This was chosen to facilitate close collaboration with computational partners at TAMU, who had to build and validate meshes for each configuration, and chose to focus on the 4-fin geometries first. The models were placed in the same reference configurations as the 4-fin models, but the alignment between the fore-bodies and the fin sections made a difference between the 3 and 4-fin models.

The heat flux maps in Figure 3.27 show a quick synopsis of the entire investigation of the 3-fin models. The 3-fin models in all 4 cases were incredibly symmetric. This likely meant that the alignment in the yaw direction was coincidentally close to 0° with respect to the free stream. Alternatively, this could indicate that the paths of the vortices were less sensitive to yaw than they

were on the 4-fin models. However, there was a radical difference between the ACE and M6QT runs that is most likely not due to unit Reynolds number alone. The AoA sweep on the 4-fin models would suggest that the models were at a positive AoA in the M6QT. The $\Delta AoA = 1^{\circ}$ case led to the horseshoe vortices moving entirely onto the fins. Due to the same sting and model alignment being used in ACE and M6QT, a misalignment of this magnitude is unlikely. The transition anomaly discovered through the side window view of the 4-fin models offers a more likely explanation. The vortex heating streaks in the side view were entirely on the fin when there was turbulence on the back of the model. If the same mechanism that caused the transition on the sides of the 4-fin models was causing transition here, it may also work to keep the vortices on the fins instead of the cylinder. However, there was no clear vortex breakdown or transition region on the 3-fin models at $Re/m = 10 \times 10^6$. Further study is needed using the new models to eliminate the possibility of model asymmetry or alignment and any asymmetries in the freestream.

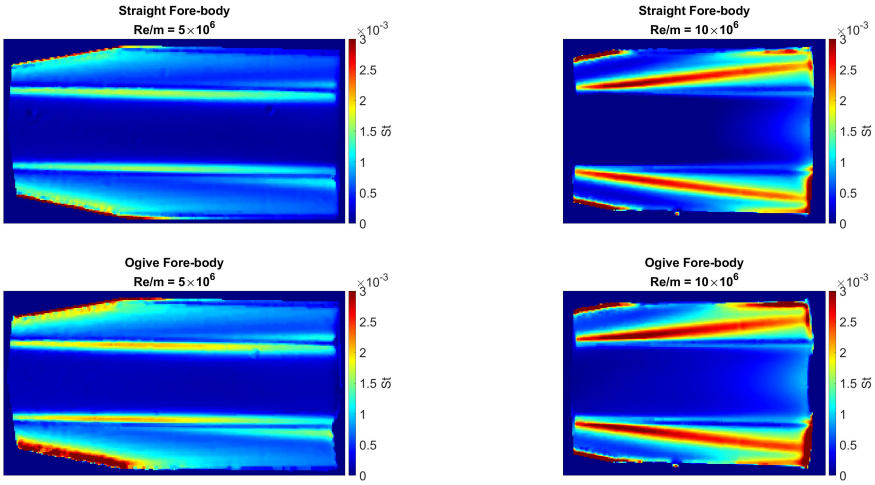

Figure 3.27: Heat flux maps for the 3-fin blockage models in ACE ($Re/m = 5 \times 10^6$) and M6QT ($Re/m = 10 \times 10^6$).

Traces of heat flux were compared at x = 0.45 m between all 4 cases using experimental and CFD data, shown in Figure 3.28. Like the 4-fin models, the fore-body had little to no impact on the location or magnitude of heating in either the CFD or experimental results. Remarkable agreement

was achieved between experiments and CFD at $Re/m = 5 \times 10^6$ on the cylinder body. Also like the 4-fin cases, the experimental heat flux on the fins was significantly higher than the CFD. This was especially true when the vortex had crossed over to the fin as in the M6QT case. It should be noted that the horseshoe vortex had crossed over by x = 0.45 m at $Re/m = 10 \times 10^6$ in the CFD results, with the peak heating being on the fins, although not nearly to the extent of the experiments. Stability analysis results of the basic states are still forthcoming and may provide some insight into the differences between the experiments and the CFD on the 3-fin models in the M6QT.

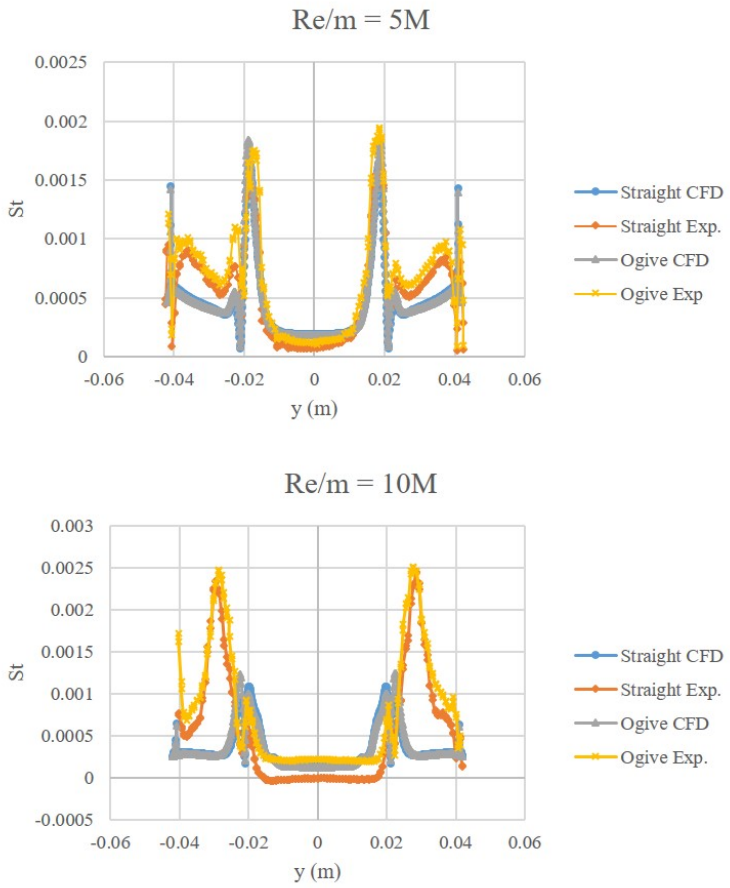

Figure 3.28: Heat flux traces from the 3-fin models at x = 0.45 m in ACE ($Re/m = 5 \times 10^6$) and M6QT ($Re/m = 10 \times 10^6$), (CFD from private correspondence with Travis S. Kocian, TAMU, 2021).

4. CONCLUSIONS AND RECOMMENDATIONS

A methodology has been developed to study fin-induced shock-boundary layer interactions in the ACE and M6QT tunnels. It includes a novel method to convert IR temperature data into heat flux using the 3D heat equation. 3D printing techniques have been developed to rapidly and affordably manufacture quality models that allow for simultaneous IR and surface pressure measurements. These tools and techniques have been used to conduct experiments on the fin-cone geometry and compared to experiments conducted using previously established techniques. Once some fidelity had been established, initial parametric studies were conducted on multi-fin models. These results pave the way for building a validation database for computational models.

The heat flux reduction tool reduces IR temperature data into non-dimensional heat flux for comparison to other experiments and flight tests using the full, 3D heat equation. The method took as its starting point the assumptions previously implemented through the 1D heat equation to reduce data from the ACE and M6QT facilities. Accurate 3D mapping and solution independence from grid size were demonstrated. The method was validated by comparison against CFD and 1D methods in regions where those methods should be accurate and improved results compared to 1D results in regions where that solution method was known to be inaccurate. The method was found to be limited by the size of the domain it could handle, as well as the significant increase in time required to reduce data. The sparseness of nodes meant that heating peaks could not always be captured unless a node happened to be exactly on the peak. However, comparison to CFD demonstrated enough detail could be shown to validate CFD solutions. The method was also limited by assumptions about the invisible sides of the fins. The consistent discrepancies between CFD and experiments on fins could be due to poor assumptions, a lack of mesh density in the fins, or a combination of both. Overall, the new 3D heat flux tool introduces a new capability that will be necessary for the study of fin-induced SBLI's and opens the door for further progress at TAMU.

A novel manufacturing method was introduced and validated for the construction of models for IR investigation and laminar to turbulence transition studies. Models were printed using Formlabs

Rigid 10K resin in multiple components. The material properties of the Rigid 10K resin were measured to allow for the conversion of temperature data into heat flux. Investigations on the fin-cone and comparison to prior experimental and CFD results on that geometry demonstrated sufficient model manufacturing quality to capture the same pressure frequencies and heat flux profiles as obtained in previous studies. This manufacturing method will significantly reduce the time and cost to obtain new models.

Initial investigations of the multi-fin models were conducted, primarily on blockage models with known asymmetric prints. To account for the difference between the effects of model alignment errors and model imperfections, the effects of model alignment were studied and sketched in Figure 4.1. In ACE at $Re/m = 5 \times 10^6$, yaw was found to dominate the location of vortex heating streaks. In M6QT at $Re/m = 10 \times 10^6$, the AoA was found to dramatically affect the flow field, with a leading edge vortex appearing in addition to the horseshoe vortex at negative AoA and the horseshoe vortex crossing entirely over to the fin in the field of view at positive AoA. The horseshoe vortex path appears to be guided by pressure gradients, crossing over from the body to the fin when that side of the fin is hidden from the freestream flow and being pushed towards the middle of the cylinder when the side of the fin is a compression face with respect to the freestream. A sweep of the unit Reynolds number showed the appearance of a leading edge vortex at $Re/m = 8 \times 10^6$, which would explain why the AoA sweep in ACE did not lead to such dramatic effects as those observed in the M6QT. When the cylinder body is a compression face relative to the freestream, it acts like the conical surface of the fin-cone and creates enough crossflow along the fin to generate a leading edge vortex. Besides generating a leading edge vortex, which may have indicated a slight AoA, increasing unit Reynolds number led to higher heating levels, promoted crossover of the horseshoe vortex, and caused the possible formation of secondary horseshoe vortices. The effects of fore-body geometry, which controls the pressure gradients in the incoming boundary layer impinging on the SBLI, had no significant effect. The effects of the number of fins are still unclear, but the behavior of the flow field appears to be very similar between the two geometries. Clearly, future work on multi-fin models will require a great deal of time aligning the models in

the tunnel and less on the geometries of the particular models.

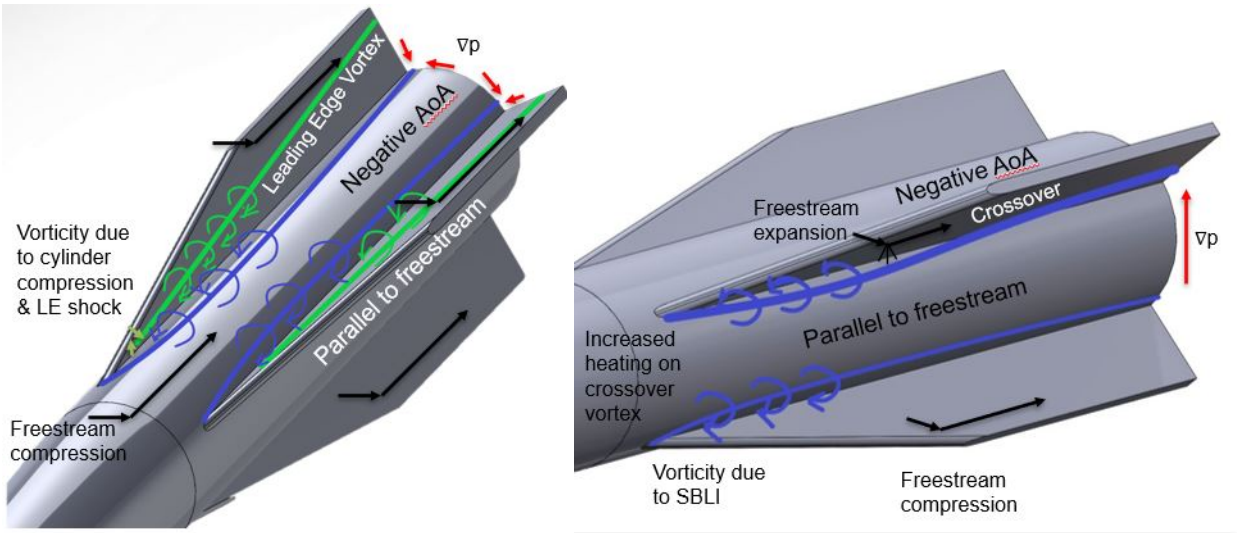

Figure 4.1: Schematic of vortices and vortex paths observed during alignment studies.

Future work will include building a reliable database on the multi-fin models as well as understanding the effects of the tunnel freestream environment. After significant effort to produce good methods of model manufacturing and an understanding of how to align the models, quality IR data may be taken after aligning the improved multi-fin models with the freestream. Additionally, pressure fluctuations should be measured in the vortices on the cylinder body to provide validation databases for stability analyses that predict the most unstable frequencies. To reduce the number of assumptions, a way should be found to gather data on both sides of the fins, to either verify the symmetry assumption or to provide measured boundary conditions to all wetted surfaces for the 3D heat equation domain. Beyond this, the effects of tunnel conditions on the SBLI must be understood. More care may need to be taken to ensure that the SBLI on future models will be generated within the quiet core. This would provide an excellent database for CFD codes and models to be validated against.

REFERENCES

[1] J. D. Pickles and V. Narayanaswamy, "Control of Fin Shock Induced Flow Separation Using Vortex Generators," *AIAA Journal*, vol. 58, no. 11, pp. 4794–4806, 2020.

[2] S. A. Craig, *Stability of High-Speed, Three-Dimensional Boundary Layers*. Phd dissertation, Texas A&M University, 2015.

[3] J. E. Green, "Interactions Between Shock Waves and Turbulent Boundary Layers," *Progress in Aerospace Sciences*, vol. 11, pp. 235–340, 1970.

[4] R. H. Korkegi, "Survey of Viscous Interactions Associated with High Mach Number Flight," *AIAA Journal*, vol. 9, no. 5, pp. 771–784, 1971.

[5] D. R. Chapman, D. M. Kuehn, and H. K. Larson, "Investigation of Separated Flows in Supersonic and Subsonic Streams with Emphasis on the Effect of Transition," *NACA Technical Report 1356*, pp. 421–460, 1957.

[6] R. H. Korkegi, "On the Structure of Three-Dimensional Shock-Induced Separated Flow Regions," *AIAA Journal*, vol. 14, no. 5, 1976.

[7] R. J. Cresci, S. G. Rubin, C. T. Nardo, and T. C. Lin, "Hypersonic Interaction Along a Rectangular Corner," *AIAA Journal*, vol. 7, no. 12, pp. 2241–2246, 1969.

[8] A. Charwat and L. Redekopp, "Supersonic interference flow along the corner of intersecting wedges," *AIAA 3rd Aerospace Sciences Meeting*, 1966.

[9] D. S. Dolling, "Fifty Years of Shock-Wave/Boundary-Layer Interaction Research: What Next?," *AIAA Journal*, vol. 39, no. 8, pp. 1517–1531, 2001.

[10] D. P. Aeschliman and W. L. Oberkampf, "Experimental Methodology for Computational Fluid Dynamics Code Validation," *AIAA Journal*, vol. 36, no. 5, pp. 733–741, 1998.

[11] J. J. Sebastian and F. K. Lu, "Upstream-Influence Scaling of Fin-Generated Shock-wave/Laminar Boundary-Layer Interactions," in *AIAA Aviation Forum*, 2020.

[12] J. D. Pickles, Balachandra, R. Mettu, P. K. Subbareddy, V. Narayanaswamy, J. D. Vasile, and J. Despirito, "Computational Modeling of Fin Induced Shock Wave/Turbulent Boundary Layer Interactions Over an Axisymmetric Surface," in *AIAA Scitech Forum*, 2020.

[13] N. B. Oliviero, T. S. Kocian, A. J. Moyes, and H. L. Reed, "EPIC: NPSE Analysis of Hypersonic Crossflow Instability on Yawed Straight Circular Cone," in *45th AIAA Fluid Dynamics Conference*, June, 2015.

[14] S. A. Craig and W. S. Saric, "Crossflow Instability on a Yawed Cone at Mach 6," *Procedia IUTAM*, vol. 14, pp. 15–25, 2015.

[15] J. Hofferth, W. Saric, J. Kuehl, E. Perez, T. Kocian, and H. Reed, "Boundary-Layer Instability and Transition on a Flared Cone in a Mach 6 Quiet Wind Tunnel," *International Journal of Engineering Systems Modelling and Simulation*, vol. 5, no. 1-3, pp. 109–124, 2013.

[16] T. S. Kocian, E. Perez, N. B. Oliviero, J. J. Kuehl, and H. L. Reed, "Hypersonic Stability Analysis of a Flared Cone," in *51st AIAA Aerospace Sciences Meeting including the New Horizons Forum and Aerospace Exposition*, AIAA 2013-0667.

[17] F. D. Turbeville and S. P. Schneider, "Boundary-Layer Instability on a Slender Cone with a Highly Swept fin," in *AIAA Fluid Dynamics Conference*, 2018.

[18] D. Mullen, A. J. Moyes, T. S. Kocian, and H. L. Reed, "Heat Transfer and Boundary-Layer Stability Analysis of Subscale Bolt and the Fin Cone," in *AIAA Aviation Forum*, 2019.

[19] F. D. Turbeville and S. P. Schneider, "Transition on a Cone with a Highly-Swept Fin at Mach 6," in *AIAA Aviation Forum*, 2019.

[20] A. L. Knutson, G. S. Sidharth, and G. V. Candler, "Direct Numerical Simulation of Mach 6 Flow Over a Cone with a Highly Swept Fin," in *AIAA Aerospace Sciences Meeting*, 2018.

[21] J. B. Edelman and S. P. Schneider, "Secondary Instabilities of Hypersonic Stationary Crossflow Waves," *AIAA Journal*, vol. 56, no. 1, pp. 182–192, 2018.

[22] A. L. Knutson, G. S. Sidharth, and G. V. Candler, "Instabilities in Mach 6 Flow Over a Cone with a Swept Fin," in *AIAA Fluid Dynamics Conference*, 2018.

[23] A. L. Knutson, *Numerical Simulation of Instabilities in Three-Dimensional Hypervelocity Boundary Layers*. Phd thesis, Minnesota, 2020.

[24] H. E. Kostak, *Ground Test Analyses of the AFOSR Boundary Layer Transition (BOLT) Flight Geometry*. Masters thesis, Texas A&M University, 2020.

[25] J. Hofferth, *Boundary-Layer Stability and Transition on a Flared Cone in a Mach 6 Quiet Wind Tunnel*. PhD thesis, 2013.

[26] E. K. Benitez, J. S. Jewell, and S. P. Schneider, "Separation Bubble Variation Due to Small Angles of Attack for an Axisymmetric Model at Mach 6," in *AIAA Scitech Forum*, 2021.

[27] A. N. Leidy, I. T. Neel, N. R. Tichenor, R. D. Bowersox, and J. D. Schmisseur, "Some Effects of Tunnel Noise on Cylinder-Induced Mach 6 Transitional Shock Wave Boundary Layer Interactions," in *AIAA Scitech Forum*, 2020.

[28] J. W. Hofferth, R. D. Bowersox, and W. S. Saric, "The Mach 6 Quiet Tunnel at Texas A&M: Quiet Flow Performance," in *27th AIAA Aerodynamic Measurement Technology and Ground Testing Conference*, 2010.

[29] J. P. Sullivan, S. P. Schneider, T. Liu, J. Rubal, C. A. C. Ward, J. J. Dussling, C. Rice, R. Foley, Z. Cai, B. Wang, and S. Woodiga, "Quantitative Global Heat Transfer in a Mach-6 Quiet Tunnel," *NASA Cr-2012-217331*, 2012.

[30] A. N. Leidy, *An Experimental Characterization of 3-D Transitional Shock Wave Boundary Layer Interactions at Mach 6*. Phd dissertation, Texas A&M, 2019.

[31] I. T. Neel, *Influence of Environmental Disturbances on Hypersonic Crossflow Instability on the HIFiRE-5 Elliptic Cone*. Phd dissertation, Texas A&M University, 2019.

[32] C. F. Boyd and A. Howell, "Numerical Investigation of One-Dimensional Heat-Flux Calculations," tech. rep., Naval Surface Warfare Center, 1994.

[33] I. T. Neel, A. N. Leidy, N. R. Tichenor, and R. D. Bowersox, "Influence of Environmental Disturbances on Hypersonic Crossflow Instability on the HIFiRE-5 Elliptic Cone," in *AIAA Aerospace Sciences Meeting*, 2018.

[34] T. J. Juliano, L. A. Paquin, and M. P. Borg, "HIFiRE-5 Boundary-Layer TransitionMeasured in a Mach-6 Quiet Tunnel with Infrared Thermography," *AIAA Journal*, vol. 57, no. 5, pp. 2001–2010, 2019.

[35] D. G. Walker and E. P. Scott, "Evaluation of Estimation Methods for High Unsteady Heat Fluxes from Surface Measurements," *Journal of Thermophysics and Heat Transfer*, vol. 12, no. 4, pp. 543–551, 1998.

[36] M. Zaccara, S. Cerasuolo, G. Cardone, J. B. Edelman, and S. P. Schneider, "Infrared Thermography Data Reduction Technique for Heat Transfer Measurements in the Boeing/AFOSR Mach-6 Quiet Tunnel," in *AIAA Scitech Forum*, 2019.

[37] J. W. Hofferth, R. A. Humble, D. C. Floryan, and W. S. Saric, "High-Bandwidth Optical Measurements of the Second-Mode Instability in a Mach 6 Quiet Tunnel," in *51st AIAA Aerospace Sciences Meeting including the New Horizons Forum and Aerospace Exposition*, pp. 1–14, 2013.

[38] J. W. Hofferth and W. S. Saric, "Boundary-Layer Transition on a Flared Cone in the Texas A&M Mach 6 Quiet Tunnel," in *50th AIAA Aerospace Sciences Meeting Including the New Horizons Forum and Aerospace Exposition*, 2012.